# High Fidelity Thrust Model For Solar Photon Sailing

*Author:*
Tommaso Pino

*Supervisor:*
Christian CIRCI

*A thesis submitted*
*in partial fulfilment of the requirements*
*for the degree of*
*Doctor of Philosophy*
*in the subject of*
*Aeronautical and Space Engineering*

Sapienza Università di Roma
Department of Mechanical and Aerospace Engineering

## Abstract

Taking into consideration the importance of a detailed model in the trajectory propagation, three space missions using solar photon sailing has been studied with a different thrust models. Then, an equipment has been designed and built to measure the deformation of a real sample of solar sail on several work conditions. An analysis of the deformations and they distributions has been taken in account to extrapolate a more accurate model for thrust. A comparison between models in function of the sail parameters has been presented to compare the optimal time of travel to reach a circular-to-circular orbital change.

## Acknowledgments

An experimental research project is a minefield made of unexpected events, de-motivation and despair. We often ask ourselves if we are proceeding in the right direction. You find yourself wandering in the fog convinced that there is a mountain to climb in front of you ... the problem is that you do not know where it is.

The people I will go to thank are those who supported me, but above all endured, in these difficult moments. They are the ones I thank for helping me to live the wonderful emotions I felt when the instrument started to proceed from planning to realization. The pride and satisfaction in observing the first image reproduced on the computer of the scanned surface have repaid years of doubts.

My half, Federica, played a difficult part in all this. My bewilderment and frustration often resulted in the scorbutity that spilled over her. Thanks baby for helping me. Thank you for resisting those six months away while I was in Japan to deepen my knowledge on low-thrust optimization. Thank you, above all, for coming to see me and for sharing these three years of training with me.

Ennio ... colleague during the magistral that has always been a source of constructive envy. I always said to myself during my studies: "but if Ennio did it, then I do not see why I can not do it". Then we met together during the doctorate and with him I shared moments of fatigue and loss, but also of satisfaction and success. From colleagues we became friends and we shared a lot in the laboratories of via Salaria (above all moments of pure madness).

Vincenzo who has always raised my spirits between a coffee break and another.

My friends, who, when we meet, always manage to talk about something else and manage to distract me as only they can do.

Andrea as a student you became the figure X in our laboratory, always ready to ask a question or help me solve the riddles that mad Ennio offers us his moments of madness.

To my father and mother, who gave me the chance and the tools to get up to this level. They have always helped me, directly or indirectly, to finally reach this important title.

To you, aunt Elena, that you left us before seeing this goal, but in which you have always believed. You always gave me a little push to motivate me to keep going.

To my sisters who have made fun of me, and continue to do so, for every strange phrase I say when I try to explain my work to you. You make me laugh, I love you.

Yuichi, Christian, Giovanni and Emiliano, guides who with their advice and tips, but also with reproach and insults, have helped me to grow and complete my education.

To Nicola, Stefano, Mattia, Takuya, Javier, Ralf and all the colleagues in Japan who made me company and with whom I laughed and visited adventures in the land of the Rising Sun.

The scholars (Andrea D., Alessandro, Alina, Alessio, Andrea C., Julia, Marco and all the others) who have asked me for help, giving me a welcome distraction. I hope I have given you a concrete hand guys.

And finally I would like to thank all those who have forgotten, knowing that I know that I did not because of malice but only for personal nature.

I dedicate this work to you all and thank you for your help.

Now if you want, you can pretend to read the thesis or say that you did, in both cases I will pretend to believe you.

# Ringraziamenti

Un progetto di ricerca sperimentale che si rispetti é un campo minato fatto di imprevisti, demotivazione e sconforto. Spesso ci si chiede se si sta procedendo nella giusta direzione. Ti trovi a vagare nella nebbia convinto che davanti a te ci sia una montagna da scalare ... il problema é che non sai dove questa sia.

Le persone che andró a ringraziare sono quelle che mi hanno supportato, ma sopratutto sopportato, in questi momenti difficili. Sono loro che ringrazio per avermi aiutato a vivere le stupende emozioni che ho provato quando lo strumento ha iniziato a procedere dalla progettazione alla realizzazione. L'orgoglio e la soddisfazione nell'osservare la prima immagine riprodotta al computer della superficie scansionata hanno ripagato anni di dubbi.

La mia metá, Federica, ha giocato una parte difficile in tutto questo. Il mio smarrimento e frustrazione spesso sono sfociate in scontrositá che si é riversata su di lei. Grazie piccola di avermi aiutato. Grazie di aver resistito quei sei mesi di distanza mentre io ero in Giappone ad approfondire le mie conoscenze sull'ottimizzazione in bassa spinta. Grazie sopratutto di essermi venuta a trovare e di aver condiviso con me questi tre anni di formazione.

Ennio ... collega durante la magistrale che é sempre stato fonte di una invidia costruttiva. Mi dicevo sempre durante gli studi: "ma se lo ha fatto Ennio, allora non vedo perché non lo possa fare io". Poi ci siamo ritrovati insieme durante il dottorato e con lui ho condiviso momenti di fatica e di smarrimento, ma anche di soddisfazione e di successo. Da colleghi siamo diventati amici e abbiamo condiviso moltissimo nei laboratori di via Salaria (sopratutto momenti di pura pazzia).

Vincenzo che tra una pausa caffé e l'altra mi ha sempre sollevato il morale.

I miei amici, i quali, quando ci vediamo, riescono sempre a parlare di altro e riescono a distrarmi come solo loro riescono a fare.

Andrea che da studente sei diventato la figura X nel nostro laboratorio, sempre pronto a fare una domanda o ad aiutarmi a risolvere gli indovinelli che quel folle Ennio ci propone dei suoi momenti di follia.

A mio padre e mia madre che mi ha dato la possibilitá e gli strumenti per arrivare fino a questo livello. Loro mi hanno aiutato sempre, direttamente o indirettamente, per raggiungere infine questo importante titolo.

A te zia Elena, che ci hai lasciati prima di vedere questo traguardo, ma nel quale hai sempre creduto. Mi hai sempre dato una spintarella per motivarmi ad andare avanti.

Alle mie sorelle che mi hanno preso in giro, e continuano a farlo, per ogni frase strana che dico quando provo a spiegare loro il mio lavoro. Mi fate tanto ridere, vi voglio bene.

Yuichi, Christian, Giovanni e Emiliano, guide che con i loro consigli e dritte, ma anche con rimproveri e improperi, mi hanno aiutato a crescere e a completare la mia formazione.

A Nicola, Stefano, Mattia, Takuya, Javier, Ralf e tutti i colleghi del Giappone che mi hanno fatto compagnia e coi i quali ho riso e vissuto avventure nel paese del Sol levante.

I tesisti (Andrea D., Alessandro, Alina, Alessio, Andrea C., Giulia, Marco e tutti gli altri) che mi hanno chiesto aiuto concedendomi una gradita distrazione. Spero di avervi dato una mano concreta ragazzi.

Ed infine vorrei ringraziare tutti coloro che ho dimenticato, che conoscendomi sapranno che non l'ho fatto per cattiveria ma solo per natura personale.

A tutti voi dedico questo lavoro e vi ringrazio.

Ore se avete voglia, potete far finta di leggere la tesi oppure dire che lo avete fatto, in entrambi i casi faró finta di credervi.

# Contents

**Abstract** **i**

**Acknowledgments** **ii**

**Ringraziamenti** **iv**

**1 Introduction** **1**

**2 Well to Know** **5**
- 2.1 Solar Photon Sailing . . . . . . . . . . . . . . . . . . . . 5
  - 2.1.1 Thrust Models . . . . . . . . . . . . . . . . . 6
  - 2.1.2 Deformations . . . . . . . . . . . . . . . . . . 8
  - 2.1.3 Attitude definition . . . . . . . . . . . . . . . 9
- 2.2 Dynamical Models . . . . . . . . . . . . . . . . . . . . . 10
  - 2.2.1 Two-body problem . . . . . . . . . . . . . . . 10
  - 2.2.2 Three-body problem . . . . . . . . . . . . . . 12
  - 2.2.3 N-body problem . . . . . . . . . . . . . . . . 16
- 2.3 Optimization . . . . . . . . . . . . . . . . . . . . . . . 19

**3 Low Thrust Trajectory Optimization** **23**
- 3.1 Alpha Centauri Tour analysis . . . . . . . . . . . . . . . 23
  - 3.1.1 Alpha Centauri System . . . . . . . . . . . . . 24
  - 3.1.2 Equation of motion . . . . . . . . . . . . . . . 26
  - 3.1.3 Numerical simulations . . . . . . . . . . . . . 27
    - Capture phase . . . . . . . . . . . . . . . . . 28
    - Polar orbit about Alpha Centauri A . . . . . . . . 30
    - Transfer trajectory from $\alpha$CenA to $\alpha$CenB . . . . 31
    - Polar orbit about Alpha Centauri B . . . . . . . . 32
  - 3.1.4 Zero Velocity Curves analysis . . . . . . . . . 33
- 3.2 Early Warning Mission . . . . . . . . . . . . . . . . . . 37
  - 3.2.1 Statement of the problem . . . . . . . . . . . . 38
  - 3.2.2 Conjecturing a sailcraft for CME surveillance . . . 42
  - 3.2.3 Nominal orbital synchronization . . . . . . . . . . 45

Synchrony loss . . . . . . . . . . . . . . . . . . . . . . . 45
Controlled orbit . . . . . . . . . . . . . . . . . . . . . . 47
3.3 Earth-to-Mercury and Earth-to-Mars . . . . . . . . . . . . . 51
3.3.1 Earth to Mercury . . . . . . . . . . . . . . . . . . . . 52
3.3.2 Earth to Mars . . . . . . . . . . . . . . . . . . . . . . 54
3.4 Considerations . . . . . . . . . . . . . . . . . . . . . . . . 57

**4 High Fidelity Thrust Model** **59**
4.1 Instrument setup . . . . . . . . . . . . . . . . . . . . . . . 60
4.2 Samples preparation . . . . . . . . . . . . . . . . . . . . . 62
4.3 Experimental Acquisition Campaign . . . . . . . . . . . . . . 65
4.4 Experimental Analysis . . . . . . . . . . . . . . . . . . . . 67
4.5 Deterministic comparation . . . . . . . . . . . . . . . . . . 69

**5 Conclusions** **73**

**A Appendix A** **76**

**Bibliography** **85**

# List of Figures

2.1.1 Azimuth, elevation and normal vector in the Orbital Reference System. . . . . . . . . . . . . . . . . . . . . . . . 10
2.2.1 R3BP reference frame . . . . . . . . . . . . . . . . . . . . . 13

3.1.1 A/B orbital plane with respect to the mean ecliptic at J2000. 25
3.1.2 Sun direction in BSRS. . . . . . . . . . . . . . . . . . . . . 26
3.1.3 Capture trajectory about $\alpha$CenA in BFRS. . . . . . . . . 29
3.1.4 Polar circular orbit about $\alpha$CenA in BFRS. . . . . . . . . 30
3.1.5 The inclination variation about $\alpha$CenA. . . . . . . . . . . 30
3.1.6 Transfer trajectory from $\alpha$CenA to $\alpha$CenB in BFRS. . . 32
3.1.7 Changing inclination manoeuvre about $\alpha$CenB . . . . . . 33
3.1.8 ZVC during the capture manoeuvre about $\alpha$CenA . . . . 35
3.1.9 ZVC during the transfer trajectory from $\alpha$CenA to $\alpha$CenB 36
3.2.1 Contours of the period of a general Keplerian orbit as function of the semi-major axis (AU) and the radial lightness number . . . . . . . . . . . . . . . . . . . . . . . . . . 39
3.2.2 Contour lines of the sail side as function of the warning time and the gross payload mass. . . . . . . . . . . . . . 40
3.2.3 (a) sailcraft drifting, under the gravitational disturbances of the Earth-Moon system (mainly), Jupiter, and Venus, as it would appear in EMB-HOF. At epoch, the vehicle is synchronous with the Earth-Moon barycentre. (b) sailcraft's angular evolution as observed in EMB-HOF. . . . 46
3.2.4 Evolution of the sailcraft described by Eq. (3.2.12) driven by the piece-wise control reported in Tab. 3.2.2. The curves on parts (a) and (b) should be compared with Fig. 3.2.3 . . . . . . . . . . . . . . . . . . . . . . . . . . 50
3.3.1 The concept of the mission under analysis, the dashed curves are the planet's orbit and the continuous lines are the sailcraft trajectories . . . . . . . . . . . . . . . . . . 51
3.3.2 Mercury's trajectory comparison for $a_c = 0.3 mm/s^2$ . . 52
3.3.3 Mercury's trajectory comparison for $a_c = 0.5 mm/s^2$ . . 53
3.3.4 Mercury's trajectory comparison for $a_c = 0.7 mm/s^2$ . . 53

3.3.5 Time of flight for Specular and Optical model in function of characteristic acceleration $a_c$ . . . . . . . . . . . . . . 54
3.3.6 Time of flight for Specular and Optical model in function of sail loading $\sigma$ . . . . . . . . . . . . . . . . . . . . . . . . . 54
3.3.7 Mars's trajectory comparison for $a_c = 0.3mm/s^2$ . . . . 55
3.3.8 Mars's trajectory comparison for $a_c = 0.5mm/s^2$ . . . . 55
3.3.9 Mars's trajectory comparison for $a_c = 0.7mm/s^2$ . . . . 56
3.3.10 Time of flight to Mars for Specular and Optical model in function of characteristic acceleration $a_c$ . . . . . . . . . 56
3.3.11 Time of flight to Mars for Specular and Optical model in function of sail loading $\sigma$ . . . . . . . . . . . . . . . . 56

4.1.1 Reference frame of the equipment . . . . . . . . . . . . . 60
4.1.2 Moveable platform to apply tension to the samples . . . . 61
4.1.3 Photo of the equipment . . . . . . . . . . . . . . . . . . . 62
4.2.1 Generic sample during application of Kapton support . . 63
4.2.2 Sample's details of the eyelets (white ring) and the Kapton support (opaque area) with and without tension . . . . . 63
4.2.3 Packaging degradation process . . . . . . . . . . . . . . . 64
4.3.1 Starting load, with the identifier of tensional platforms . 65
4.4.1 PDF azimuthal . . . . . . . . . . . . . . . . . . . . . . . . 67
4.4.2 PDF zenithal . . . . . . . . . . . . . . . . . . . . . . . . . 68
4.4.3 Comparation of PDFs' zenithal for all three samples . . . 68
4.5.1 Time of flight for Specular, Optical and Optical Deformed model in function of ideal sail loading $\sigma_0$ . . . . . . . . . 70
4.5.2 Time of flight for Specular, Optical and Optical Deformed model in function of real sail loading $\sigma_w$ . . . . . . . . . 71

# List of Tables

2.1.1 CP1 optical parameters for the full spectrum . . . . . . . 7

3.1.1 $\alpha$CenA and $\alpha$CenB principal characteristics . . . . . . . 24
3.1.2 Release condition values . . . . . . . . . . . . . . . . . 28
3.1.3 Arc duration and attitude angles in ORS during the capture trajectory . . . . . . . . . . . . . . . . . . . . . . . . 29
3.1.4 Attitude angles in ORS during the out of plane trajectory about $\alpha$CenA . . . . . . . . . . . . . . . . . . . . . 31
3.1.5 Attitude angles in ORS during the transfer trajectory from $\alpha$CenA to $\alpha$CenB. . . . . . . . . . . . . . . . . . . 32
3.1.6 Attitude angles in ORS during the out of plane trajectory about $\alpha$CenA . . . . . . . . . . . . . . . . . . . . . 34
3.2.1 Example of sailcraft that satisfies the concept of early-warning sail well below in radial distance than the Sun-Earth system L1 . . . . . . . . . . . . . . . . . . . . . . . . 44
3.2.2 Control parameters that synchronize the sailcraft orbit from 2022-07-05 to 2023-07-05 in the sense of Eq. (3.2.12). Arc-0 denotes the end-point of the transfer trajectory that moves the sailcraft from the injection point (on the Earth's outer sphere of influence) to the first nominal station point. 49

4.3.1 Summarize of all tension's cases for each vertexes . . . . 67
4.5.1 Effects of Area's deviation ($\delta A$) and/or normal's deviation ($\delta \mathbf{n}$) on Fresnel optimal trajectory for three different values of characteristic acceleration $a_{c0}$ . . . . . . . . . . . . . 70

Everyone knew it was impossible,
until a fool who didn't know
came along and did it.
Cit. **Albert Einstein**

# 1

# Introduction

Sailing in space is an ancient dream and an idea that goes back to the 1600 with Johannes Kepler, even if the majority of the scientist were sceptical about this kind of propulsion. Going back in time, we should remember that only in 1783 the Montgolfier brothers with their balloons have made the very first human fly and only later in 1903 when the Wright brothers build Orville, the world's first successful flying machine making the first controlled, powered and sustained heavier-than-air human flight. The technology of that time was not able to achieve space flight and a voyage from the earth to the moon was only possible in the fervid imagination of the French science fiction writer Jules Verne. His dream will become a reality later on, when the German born aerospace engineer and spacecraft architect Wernher von Braun and his team developed the Saturn V rocket that propelled the Apollo spacecraft to the Moon. Nowadays ordinary people regularly fly from one continent to another and a space station is available to the scientific research of developed country, but the aspiration of the human being is far to be satisfied, and a new frontiers in and out of the solar system is foreseen. Unfortunately, as happened in the past, the current space technology, based on propellant rockets, cannot fulfil the requirements needed to reach future goals.

As in the past, technological research has to find a new kind of propulsion for travelling and eventually escape from the solar system. A promising new engine, able to fulfil the requirements of space missions is a remake of the old Kepler dream of sailing the space by using a solar sail pushed by solar radiation pressure. Recently, the current still strong scepticism around this propulsive engine do not has demotivated the scientists of the Japanese space agency who in 2010 launched the IKAROS space mission with the intend to reach Venus using only a solar sail with the solar radiation pressure as the unique propulsive system and sail likewise a sailing boat. The mission was a complete success with the flyby of the planet obtained the same year. Such an important result has stimulated the majority of the space scientific community around the study of new kinds of missions that cannot be realized by mean of classical rockets. Nowadays, the preliminary analysis of any mission of this kind is mainly made by using a three-body model considering two massive objects that are moving around the common center of mass, with Keplerian's orbits, and a third body of negligible mass free of moving within the influence of the gravitational field generated by those two masses. This model can be in the simple form, where the primary orbits are assumed as circular, or in a more general form considering the presence of an eccentricity. Otherwise a full ephemeris dynamical model is considered to better approximate the trajectory designed. Regardless of the dynamical model, the acceleration generated by a solar sail plays a predominant role in governing the dynamical evolution of a sailcraft. Object of this thesis is the analysis of the general reflection models of a solar sail with the determination of known and unknown informations, to better understand the effects on the solar sail's thrust efficiency.

In Chap. 2 an overview of optimisation methods and solar photon sailing reflection models is made.

Several deterministic missions are analysed in Chap. 3 using different dynamic models. First of all, a mission to Alpha Centauri where a specular reflection model in an elliptic three body problem with two emitting body is considered in all star system phases [1]. The Coronal Mass Ejection early warning is presented in the second section of Chap. 3. The synchronism problem between the Earth-Moon barycentre and a probe with a semi major axis less than an astronomical unit is explained at first and then how to solve it using a solar sail that faces all the time in the Sun direction [2]. Lastly a parametric problem is presented to analyse the difference using two distinguish reflection models. The missions selected are a circular-circular planar orbital transfer from Earth to Mercury and Earth to Mars, with perfect and Fresnel reflection models.

In Chap. 4 the problem of sail's membrane wrinkling is presented. It can be mainly ascribed to (a) *wrinkles*, i.e. elastic response of the membrane to compressive stress and/or strain, and (b) *creases*, i.e. inelastic response as a result of folding and/or handling (mainly), especially when the membrane is coated by a thin metal film. Nevertheless, our concern in that chapter is to - much more simply - try to evaluate the impact of wrinkles and creases collectively onto the final orbital state of a sailcraft in the simple orbital transfer presented lastly in Chap. 3. Normally, the preliminary trajectory design of a sailcraft from the post-deployment state to the chosen space target assumes a sufficiently flat sail, which is irradiated by the solar electromagnetic waves. An equipment described in Chap. 4 has been designed and built to analyse the deformations of several solar sail samples. A statistical analysis is conducted and taking in consideration the last mission analysed we compare the effect of that deformation respect a flat sail surface.

Chap. 5 summarizes the conclusions of this work and outline suggestions for future research.

# 2

# Well to Know

In this chapter we will present the concepts required in the rest of the thesis. Low thrust propulsion system is presented introducing the solar photon sailing system. Three light reflection models are presented to empathize the differences between each one. It is also presented the deformations problem and how it affects the lightness vector, the aim of the thesis. Space dynamical models are introduced from the two body problem to the N body problem. Finally, a short introduction to the optimization methods (focusing on the direct one) is performed.

## 2.1 Solar Photon Sailing

The solar photon sailing thrust is a really new kind of space propulsion system and it differs from all others used in the space sector. The main characteristic that makes it interesting is that, this propulsion system, is not produced by the ejection of propellant, but using the solar radiation pressure, in particular, the photons momentum contents in the light, coming from the star. Moreover, assuming a very long life duration of a star, it is correct to consider it as an unlimited and continuous source of energy. The only limit of this kind of space propulsion is given by the degradation of the sail materials and the necessity to have a star nearby. The availability of solar photon sails, make possible a new class of space missions otherwise impossible to realize using chemical propulsion [3, 4]. Some examples of these missions are: rendez-vous with comets, meteors or asteroids [5]; classical interplanetary transfers [6]; missions for exploration and analysis of the heliopause [7]; deep exploration of interstellar space [8]; visits to other planetary system [1, 9, 10].

### 2.1.1 Thrust Models

From the beginning of the idea to use the photon momentum to provide acceleration to a sort of spacecraft, the solar sail, they started to find a model to describe how the sun light interact with the sail surface. Like always happen in every field of physics, the first model designed to describe the phenomena is the simplest one and then with the grown of knowledges increasing the complexity.

Specular reflection is the simplest model where the sunlight is completely reflected with the same incident angle $\theta_\odot$ without any lost of energy. The Eq. (2.1.1) shows how to obtain for this model the lightness vector $\mathbf{L}$, the dimensionless ratio between the solar radiation pressure vector and the Sun's local gravity. We have to introduce the critical sail loading $\sigma_{(cr)}$ as the sail loading that permits to have a unitary lightness number and assuming $1361\,W/m^2$ for the Total Solar Irradiance (TSI) $\sigma_{(cr)} = 1.531\,\frac{g}{m^2}$ [2], $\sigma$ represents the sail loading and $\mathbf{n}$ is the sail axis direction in the semi-space opposite to the Sun.

$$\mathbf{L} = \frac{1}{2}\frac{\sigma_{(cr)}}{\sigma}\cos\theta_\odot\left[2\cos\theta_\odot\mathbf{n}\right] \tag{2.1.1}$$

After all, materials and phenomenas are not perfect, indeed not all the sunlight is specular reflected. Under the optical theory proposed by [11], different contribution exist that they reduce the thrust. A quantity $\mathrm{s} < 1$ of photons continue to follow the previous model, but a diffusive and emission by re-radiation.

$$\mathbf{L} = \frac{1}{2}\frac{\sigma_{(cr)}}{\sigma}\cos\theta_\odot\left[\begin{array}{l}\left(2\mathrm{R_s s}\cos\theta_\odot + \overline{\chi}^{(\mathrm{f})}\mathrm{R_s}\left(1-\mathrm{s}\right) + \left(1-\mathrm{R_s}\right)\kappa_{(sail)}\right)\mathbf{n} \\ +\left(1-\mathrm{R_s s}\right)\mathbf{u}\end{array}\right] \tag{2.1.2}$$

Where $\mathrm{R}_s$ and $\overline{\chi}^{(j)}$ , $j =$ 'f', 'b' are the specular reflectance and the coefficient of emissive momentum [12], respectively. The $\mathbf{u}$ denote the sunlight direction, and finally the coefficient $\kappa_{(sail)}$ is

$$\kappa_{(sail)} \equiv \left.\frac{\overline{\chi}^{(\mathrm{f})}\varepsilon^{(\mathrm{f})} - \overline{\chi}^{(\mathrm{b})}\varepsilon^{(\mathrm{b})}}{\varepsilon^{(\mathrm{f})} + \varepsilon^{(\mathrm{b})}}\right|_{\mathrm{T}_{(sail)}} \tag{2.1.3}$$

The emittances of the sail front-side and back-side are denoted by $\varepsilon^{(\mathrm{f})}$ and $\varepsilon^{(\mathrm{b})}$, respectively; they are meant at the sail's equilibrium temperature [12]. Increasing the complexity of the phenomena we overcome the ideal reflectance by the well-known Fresnel reflection/absorption. Fresnel's formulae represent a vector reflection theory that permits to consider the vectorial scattering of electromagnetic radiation on a surface with low roughness. The Eq. (6.136) of [12] is the generalized equation to calculate the lightness vector for any flat sail covered by a reflective metal film and it is below reminded:

$$\mathbf{L} = \tfrac{1}{2}\tfrac{\sigma_{(cr)}}{\sigma}\cos\theta_\odot \left[ \begin{array}{l} \left(2\mathrm{R_s}\cos\theta_\odot + \chi_{(\mathrm{re})}\mathrm{R_d}\sin\beta + \mathrm{A}^{(\mathrm{f})}\kappa_{(sail)}\right)\mathbf{n} \\ + \left(\mathrm{A}^{(\mathrm{f})} + \mathrm{R_d}\right)\mathbf{u} - \chi_{(\mathrm{re})}\mathrm{R_d}\cos\beta\mathbf{x}_s \end{array} \right]$$

$$\equiv \tfrac{\sigma_{(cr)}}{\sigma}\eta\mathbf{U}$$

$$\mathbf{x}_s \equiv \begin{cases} \frac{\mathbf{u}-\cos\theta_\odot\mathbf{n}}{\sin\theta_\odot} & ,\theta_\odot > 0 \\ \text{arbitrary} & ,\theta_\odot = 0 \end{cases} \quad , \quad \mathbf{U}\cdot\mathbf{U} = 1$$

$$\mathrm{R_s} + \mathrm{R_d} + \mathrm{A}^{(\mathrm{f})} = 1 \tag{2.1.4}$$

where the following meaning of the symbols: $\mathbf{U}$ is the direction of $\mathbf{L}$ and $\eta$ is the thrust efficiency. The symbol $\chi_{(\mathrm{re})}$ denotes the coefficient of diffuse momentum and it comes from the distribution of the scattered photon momenta. If we denote the vector sum of the scattered photon momenta by $\mathbf{p}$, the angle $\beta$ in Eq. (2.1.4) is measured from $\mathbf{x}_s$ counter-clockwise in the incidence plane: $\beta = \arccos\left(\mathbf{p}\cdot\mathbf{x}_s/|\mathbf{p}|\right)$. Finally, $\mathrm{A}^{(\mathrm{f})}$ and $\mathrm{R_d}$ are the front-side absorptance and the diffuse reflectance, respectively. Considering a solar sail made in CP1 with 100 nm of Vacuum deposited Aluminium coating, the required optical parameters of the surface provided from the material data-sheet[1] are summarized in the Tab. 2.1.1 where the symbols have the meaning explained in the previous section. For the other optical parameters we refer to the second order expansion proposed in [2] and they

**Table 2.1.1:** CP1 optical parameters for the full spectrum

| | |
|---|---|
| $\varepsilon^{(\mathrm{f})}$ | 0.106 |
| $\varepsilon^{(\mathrm{b})}$ | 0.194 |

---

[1] `http://www.nexolvematerials.com/clear-colorless-polyimides/cp1-polyimide`

are reminded in Eq. (2.1.5).

$$\begin{array}{llllll} \mathrm{R_s} & = 0.867742 & -0.046874 & \theta_{\odot} - 0.009283 & \theta_{\odot}^2 \\ \mathrm{R_d} & = 0.058617 & +0.046872 & \theta_{\odot} + 0.0093614 & \theta_{\odot}^2 \\ \mathrm{A}^{(\mathrm{f})} & = 0.0736416 & +0.0000014 & \theta_{\odot} - 0.00007846 & \theta_{\odot}^2 \\ \chi_{(\mathrm{re})} & = 0.670328 & -0.105918 & \theta_{\odot} + 0.79637 & \theta_{\odot}^2 \\ \beta & = \pi/2 & +0.587443 & \theta_{\odot} - 0.917672 & \theta_{\odot}^2 \end{array} \tag{2.1.5}$$

But we have to empathize that the described reflection models do not consider any deformation in middle and large scale.

### 2.1.2 Deformations

One of the key points in sailcraft trajectory design is a good thrust model. Restricting ourselves to classical mechanics, an SPS thrust acceleration model should include

1. the SPS-relevant characteristics of the Sun;
2. the optical properties of the sail's reflective layer;
3. the local membrane deformations;
4. the overall sail shape under the solar radiation pressure action;
5. the sail attitude control and disturbances;
6. the degradation of the optical properties as the UV and solar-wind particles energy fluence onto the sail increases with time;
7. the fluctuations of the total solar irradiance (TSI).

For instance, points (1) and (2) are extensively described in Refs. [12–14]. Points (3) and (4) are detailed in Ref. [15] by using the membrane deformation theories, the finite-elements methodology, and modern designs of long-boom architectures. Point (5) has been facing with in a large number of papers; we cite Ref. [16] for classical approaches, and Ref. [2] for a potential photonic-device based solution. Point (6), applied to SPS, has been dealt with first at NASA Ref. [17], and, subsequently, described in Ref. [12] by a theoretical variant. Finally, point (7) has been introduced quantitatively in Ref. [18].

Sail's membrane wrinkling can be mainly ascribed as (a) *wrinkles*, i.e. elastic response of the membrane to compressive stress and/or strain, and (b) *creases*, i.e. inelastic response as a result of folding and/or handling (mainly), especially when the membrane is coated by a thin metal film. Chap.-3 of Ref. [15] is also an excellent synthesis of the many ways of dealing with the membrane wrinkling problem, as described in the many related references; such methods can be applied to solar sails. Nevertheless, our concern in this thesis is to - much more simply - try to evaluate the impact of wrinkles and creases collectively onto the final orbital state of a sailcraft in simple orbital transfers. Let us be more precise.

Normally, the preliminary trajectory design of a sailcraft from the post-deployment state to the chosen space target assumes a sufficiently flat sail, which is irradiated by the solar electromagnetic waves. In this study phase, the space mission analysts attempts to minimize the flight time and satisfying some constraints. This simple framework fits well experimental missions by small sails, say, of 1-2 hundred square meters, at most, like the sail of the sailcraft IKAROS/JAXA. Then, the mission analysts can add non-ideal features of a real sail system to the model of thrust, and analyses which are the effects on the mission trajectory. In this thesis, we use the thrust model developed in Refs. [2, 12, 17], for to the above points (1-2), and modify it to take winkles and creases (as a whole) into account for including point (3). The mathematical items of this model are discussed in the previous subsection. If we consider a generic effect due to the local surface deformations that could produce an effect on the effective area ($\delta A$) and the direction of the normal ($\delta \mathbf{n}$) it is obtainable the following equation that consider both effects:

$$\mathbf{L}_w^{(F)} = \frac{1}{2}\frac{\sigma_{(cr)}}{\sigma_0}\left(1+\frac{\delta A}{A_0}\right)\cos(\vartheta)\left(2\mathcal{R}^{(F)}\cos(\vartheta)\left(\mathbf{n}(t)+\delta\mathbf{n}\right)+\mathcal{A}^{(F)}\mathbf{u}\right) \tag{2.1.6}$$

Each contribution could be singularly evaluated putting the other one to zero. In Chap. 4 we are going to measure the quantity $\delta A$ and $\delta \mathbf{n}$ for a specific set of samples.

### 2.1.3 Attitude definition

As empathized in previous subsection the lightness vector formalism is used to express the thrust acceleration [12]. The lightness vector $\mathbf{L}$ is resolved in the Orbital Reference System (ORS). The ORS is centred on the sailcraft centre of mass, the x-axis is the radial outward direction from the star centre of mass (axis $r$), the z-axis is the direction of the orbital angular momentum of the sailcraft (axis $h$) and the y-axis completes the right-hand triad (axis $\theta$). Note that for the orbital angular momentum reversal strategy it is necessary to define an Extended ORS [12]. To express the thrust acceleration using the lightness vector formalism we can write:

$$\left.\frac{\mathbf{T}}{m}\right|_{BFRS} = \frac{\mu}{R^2}\left.\Xi\mathbf{L}\right|_{ORS} \tag{2.1.7}$$

where $\Xi$ is the transformation matrix from $ORS$ to BFRS. Regarding the force acting on the sailcraft, the lightness vector has the same direction as the backside normal and it points away from the considered star. Fig. 2.1.1 shows, the backside normal of the sail (n), the Euler azimuth angle ($\varphi$) and elevation angle ($\gamma$) necessary to define the components of the lightness vector in the ORS. The components of the lightness vector are:

$$\mathbf{L} = \mathcal{L}_{max} \cos^2 \gamma \cos^2 \varphi \begin{pmatrix} \cos\gamma\cos\varphi \\ \cos\gamma\sin\varphi \\ \sin\gamma \end{pmatrix} \begin{pmatrix} \hat{r} \\ \hat{\vartheta} \\ \hat{h} \end{pmatrix} \tag{2.1.8}$$

where $\mathcal{L}_{max}$ is the maximum sailcraft lightness number.

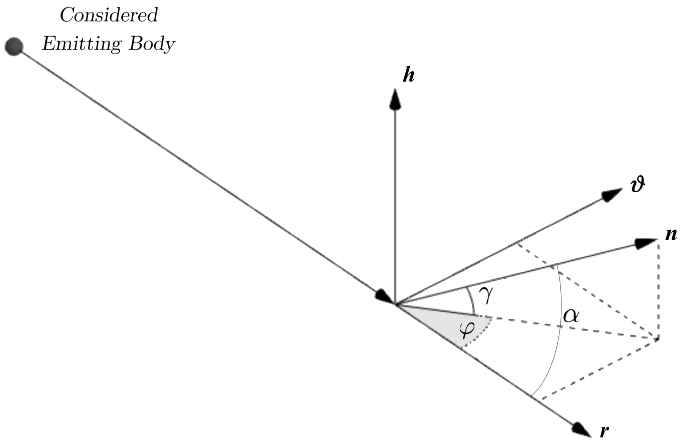

**Figure 2.1.1:** Azimuth, elevation and normal vector in the Orbital Reference System.

## 2.2 Dynamical Models

In space trajectory analysis exists several dynamical model to describe the probe's motion. The trajectory designer decide which one use depending of the accuracy of the analysis he wants performing.

### 2.2.1 Two-body problem

Considering the system composed of two singles point bodies, a primary ($M$) and a probe ($m$), isolated from the rest of the universe with masses $M \gg m$ the only acting force is the gravitational attraction.

The second dynamical law is written with constant mass, hypothesis verified for satellites but not for rockets.

$$\mathbf{F} = m\frac{d^2\mathbf{r}}{dt^2} \tag{2.2.1}$$

where $\mathbf{F}$ is the acting force, $m$ is the mass of the probe, the independent variable $t$ is time and $\mathbf{r}$ is the probe's position vector respect the primary centre of mass.

The acting force is the gravitational one:

$$\mathbf{F} = -\frac{GMm}{|\mathbf{r}|^3}\mathbf{r} = -\frac{\mu m}{|\mathbf{r}|^3}\mathbf{r} \tag{2.2.2}$$

where $G$ is the universal gravitational constant, $M$ is the mass of the primary and $\mu = GM$ is the planetary gravity constant that is chosen primary dependent.

The combination of Eqs. (2.2.1) and (2.2.2) consist into the first fundamental equation of astrodynamic:

$$\frac{d^2\mathbf{r}}{dt^2} = -\frac{\mu}{|\mathbf{r}|^3}\mathbf{r} \tag{2.2.3}$$

From Eq. (2.2.3) two primary integral are obtainable that consist into two constant quantity: angular momentum vector; Hamilton integral (eccentricity vector).

With a left multiplication of $\mathbf{r}$:

$$\mathbf{r} \times \frac{d^2\mathbf{r}}{dt^2} = 0 \tag{2.2.4}$$

and adding at the first term the null term $\frac{d\mathbf{r}}{dt} \times \frac{d\mathbf{r}}{dt}$

$$\begin{aligned}\frac{d\mathbf{r}}{dt} \times \frac{d\mathbf{r}}{dt} + \mathbf{r} \times \frac{d^2\mathbf{r}}{dt^2} &= 0 \\ \frac{d}{dt}\left(\mathbf{r} \times \frac{\mathbf{r}}{dt}\right) &= 0 \end{aligned} \tag{2.2.5}$$

Integrating we obtain immediately the angular momentum $\mathbf{h}$ for mass unit:

$$\mathbf{h} = \mathbf{r} \times \frac{d\mathbf{r}}{dt} \tag{2.2.6}$$

the plane of motion has the unit vector $\widehat{\mathbf{h}}$ and it is constant in time: the keplerian motion is planar.

Taking Eq. (2.2.3) and applying a left multiplication of **h** we obtain the second primary integral:

$$\mathbf{e} = -\hat{\mathbf{r}} - \frac{\mathbf{h}}{\mu} \times \frac{\mathbf{r}}{dt} \tag{2.2.7}$$

where we define the vector **e** as eccentricity constant in module and direction during time.

These informations permit to completely define the entire problem and obtain the keplerian trajectory (or orbit).

Adding to Eq. (2.2.3) an acceleration due to a thruster we are going to be able to modify the trajectory to achieve the design mission purpose.

$$\frac{d^2\mathbf{r}}{dt^2} = -\frac{\mu}{|\mathbf{r}|^3}\mathbf{r} + \mathbf{a} \tag{2.2.8}$$

where **a** represents the not gravitational acceleration vector if is present.

### 2.2.2 Three-body problem

When two celestial bodies are too close to each other to be considered one at a time or a continuous transfer from a primary to a secondary body wants to be performed, a definition of a more complex dynamical model is required.

In the general restricted three-body problem, an infinitesimal particle $m_3$ moves under the gravitational attraction of two primaries $M_1$ and $M_2$ ($m_3 \ll M_2 < M_1$), without affecting them. The motion of $m_3$ is usually described in a special reference frame, where the position of the primaries is fixed along the x-axis and it is positive in the direction of $M_2$, the z-axis is perpendicular to the plane of rotation and is positive upwards, and the y-axis completes the set-up in order to yield a Cartesian, rectangular, dextrose reference frame.

The small primary is orbiting the large trajectory on an elliptic orbit with eccentricity $e$. This orbit complies with two-body Keplerian motion; the distance between the primaries, $\rho$, depends upon the true anomaly, $\nu$, through the conic equation:

$$\rho = \frac{p}{(1 + e\cos\nu)} = \frac{a\left(1 - e^2\right)}{(1 + e\cos\nu)} = \frac{p}{g} \tag{2.2.9}$$

Where $p$ is the semi-latus rectum obtainable from $p = a\left(1 - e^2\right)$. The rate of change of the true anomaly satisfies $\omega = \dot{\nu} = h/\rho^2$ , where $h$ is the magnitude of the angular momentum, given by $h^2 = G\left(M_1 + M_2\right)p$ and $g = (1 + e\cos\nu)$.

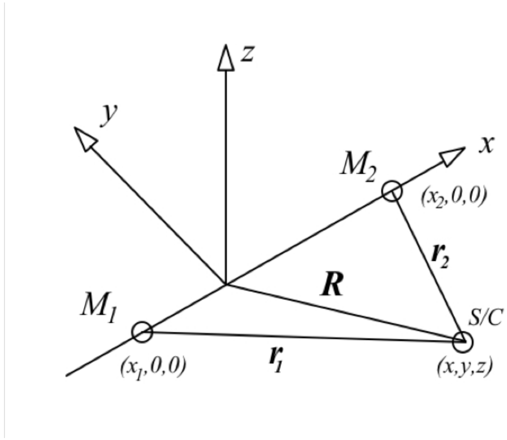

**Figure 2.2.1:** R3BP reference frame

The position vector, $\mathbf{R}$, of the sail-craft (S/C) is the rotating barycentric frame and one respect to the primaries are:

$$\begin{aligned} \mathbf{R} &= x\mathbf{i} + y\mathbf{j} + z\mathbf{k} \\ \mathbf{r_1} &= (x - x_1)\,\mathbf{i} + y\mathbf{j} + z\mathbf{k} \\ \mathbf{r_2} &= (x - x_2)\,\mathbf{i} + y\mathbf{j} + z\mathbf{k} \end{aligned} \tag{2.2.10}$$

By defining an appropriate constant it is possible to express the position of the primaries on x-axis, it is definite by:

$$\mu = \frac{M_2}{M_1 + M_2} \tag{2.2.11}$$

The position of $M_1$ is located at $[-\mu\rho, 0, 0]$ and $M_2$ at $[1 - \mu\rho, 0, 0]$. Consequentially the dynamic's equation are:

$$\left.\frac{d^2\mathbf{R}}{dt^2}\right|_{\mathrm{I}} = -\frac{\mu_1}{|\mathbf{r_1}|^3}\mathbf{r_1} - \frac{\mu_2}{|mathbfr_2|^3}\mathbf{r_2} \tag{2.2.12}$$

It is necessary to write the derives in the rotating reference frame:

$$\left.\frac{d\mathbf{R}}{dt}\right|_{\mathrm{I}} = \dot{\mathbf{R}}\Big|_{\mathrm{R}} + \boldsymbol{\omega} \times \mathbf{R}|_{\mathrm{R}} \tag{2.2.13}$$

$$\left.\frac{d^2\mathbf{R}}{dt^2}\right|_{\mathrm{I}} = \left.\Big[\ddot{\mathbf{R}} + \dot{\boldsymbol{\omega}} \times \mathbf{R} + 2\boldsymbol{\omega} \times \dot{\mathbf{R}} + \boldsymbol{\omega} \times (\boldsymbol{\omega} \times \mathbf{R})\Big]\right|_{\mathrm{R}} \tag{2.2.14}$$

And the Eq. (2.2.12) for the probe written per components in the rotating frame with a generic orbit of the secondary and primary about the common barycentre is:

$$\begin{pmatrix} \ddot{x} \\ \ddot{y} \\ \ddot{z} \end{pmatrix} + \dot{\omega} \begin{pmatrix} -y \\ x \\ 0 \end{pmatrix} + 2\omega \begin{pmatrix} -\dot{y} \\ \dot{x} \\ 0 \end{pmatrix} + \omega^2 \begin{pmatrix} -x \\ -y \\ 0 \end{pmatrix} = \tag{2.2.15}$$
$$-\frac{\mu_1}{r_1^3} \begin{pmatrix} x + \mu\rho \\ y \\ z \end{pmatrix} - \frac{\mu_2}{r_2^3} \begin{pmatrix} x - (1-\mu)\,\rho \\ y \\ z \end{pmatrix}$$

With the dynamical model written in this way we could follow two different characterization due to some hypothesis follow described: Circular Restricted 3 Body Problem (CR3BP); Elliptic Restricted 3 Body Problem (ER3BP).

CR3BP

If we consider the eccentricity equal to zero, the Sec. 2.2.2 could be significantly simplified. The angular velocity and the distance between the primaries is constant during the orbital period. This means that $\dot{\omega} = 0$ and $\rho = p$. With these assumptions the Sec. 2.2.2 becomes:

$$\begin{pmatrix} \ddot{x} \\ \ddot{y} \\ \ddot{z} \end{pmatrix} + 2\omega \begin{pmatrix} -\dot{y} \\ \dot{x} \\ 0 \end{pmatrix} + \omega^2 \begin{pmatrix} -x \\ -y \\ 0 \end{pmatrix} = \tag{2.2.16}$$
$$-\frac{\mu_1}{r_1^3} \begin{pmatrix} x + \mu \\ y \\ z \end{pmatrix} - \frac{\mu_2}{r_2^3} \begin{pmatrix} x - (1-\mu) \\ y \\ z \end{pmatrix}$$

Coming back to the vectorial notation, a potential expression could be achieved to identify the libration points.

$$\begin{aligned} \ddot{\mathbf{r}} + 2\boldsymbol{\omega} \times \dot{\mathbf{r}} &= -\frac{\mu_1}{|\mathbf{r_1}^3|}\mathbf{r_1} + \frac{\mu_2}{|\mathbf{r_2}^3|}\mathbf{r_2} + \omega^2 \mathbf{r} && (2.2.17) \\ &= \nabla \left[ \frac{\mu_1}{|\mathbf{r_1}|} + \frac{\mu_2}{|\mathbf{r_2}|} + \omega^2 \frac{(\mathbf{r} \cdot \mathbf{r})}{2} \right] && (2.2.18) \\ &= \nabla U && (2.2.19) \end{aligned}$$

$$U = \left[\frac{\mu_1}{|\mathbf{r_1}|} + \frac{\mu_2}{|\mathbf{r_2}|} + \omega^2 \frac{(\mathbf{r}\cdot\mathbf{r})}{2}\right] \tag{2.2.20}$$

where $U$ is the gravitational potential.

With a left multiplication for $\dot{\mathbf{r}}$ the term $\boldsymbol{\omega} \times \dot{\mathbf{r}}$ becomes zero for orthogonality. With few math passages a primary integral (Jacoby solution) could be achieved:

$$\frac{d}{dt}\left(\frac{V^2}{2} - U\right) = 0 \tag{2.2.21}$$

$$V^2 - 2U = 2C_2 = C_1 \tag{2.2.22}$$

where $V$ is the velocity's module. We do not enter in the calculation merit, but a five libration points named $L_i$ $(i = 1 \dots 5)$ could be identified using the potential $U$. These point are fixed in the CR3BP and they are very useful for several kind of mission. The L1 located on the x-axis between the primaries could be useful for communications or observations, a pseudo application is presented in Chap. 3. In the Earth-Sun system, the L2 located on the x-axis over the secondary is used for deep space observation.

### ER3BP

If we consider the eccentricity of the primaries' orbit transforming into the rotating-pulsing coordinates could be convenient. This transformation consists it the normalization of the time, with the quantity $\sqrt{G\left(M_1 + M_2\right)/\rho^3}$ and in normalizing the position, with the instantaneous distance $\rho$:

$$x = \rho\xi \quad y = \rho\eta \quad z = \rho\zeta \tag{2.2.23}$$

As the last step it is necessary to transform the time derivatives into derivative with respect to the true anomaly:

$$\frac{d()}{dt} = \frac{()}{d\nu}\frac{d\nu}{dt} = ()'\omega \tag{2.2.24}$$

The Appendix A summarizes all passages needed to obtain the following equation [19]:

$$\begin{cases} \xi'' & = 2\eta' + \frac{1}{g}\left(\xi - \frac{1-\mu}{|\mathbf{r_1}|^3}\left(\xi+\mu\right) - \frac{\mu}{|\mathbf{r_2}|^3}\left(\xi-1+\mu\right) - a_\xi\right) \\ \eta'' & = -2\xi' + \frac{1}{g}\left(\eta - \frac{1-\mu}{|\mathbf{r_1}|^3}\eta - \frac{\mu}{|\mathbf{r_2}|^3}\eta - a_\eta\right) \\ \zeta'' & = \frac{1}{g}\left(-e\zeta\cos\left(f\right) - \frac{1-\mu}{|\mathbf{r_1}|^3}\zeta - \frac{\mu}{|\mathbf{r_2}|^3}\zeta - a_\zeta\right) \end{cases} \tag{2.2.25}$$

where $|\mathbf{r_1}| = \sqrt{(\xi+\mu)^2 + \eta^2 + \zeta^2}$, $|\mathbf{r_2}| = \sqrt{(\xi+\mu-1)^2+\eta^2+\zeta^2}$ and if it is present in the case under consideration the $a_\xi$, $a_\eta$ and $a_\zeta$ represent the not gravitational acceleration components.

Contrary of CR3BP a closed form potential is not definable, but a pseudo potential is follow defined:

$$\Omega = 1/g\left[\frac{1}{2}\left(\xi^2+\eta^2-e\zeta\sin\nu\right) + \frac{1-\mu}{|\mathbf{r_1}|} + \frac{\mu}{|\mathbf{r_2}|}\right] \tag{2.2.26}$$

Zero Velocity Curves

In the R3BP exist forbidden regions where the energy is not conserved. In the CR3BP the Jacoby solution Eq. (2.2.22) defines a constant value if combined with the expression of the potential allows to identify the Zero Velocity Curves (ZVC) [20]. These are contour where the probe's energy is completely potential and the velocity is null. For the law of the conservation of the energy, it is not allow to go over these contour because the total energy must be higher. In Chap. 3 some example of that is presented of Alpha Centauri capture trajectory and for the transfer between system stars.

### 2.2.3 N-body problem

In a heliocentric inertial frame (HIF), the probe's barycentre moves on a curve described by the vector position $\mathbf{R}(t)$ from the Sun's center of mass to the probe barycentre, where the parameter $t$ is the Barycentric Dynamical Time (TDB) (e.g., see the IERS Technical Notes in Ref. [21]). The motion equations of a general spacecraft in HIF can be written as

$$\frac{d^2}{dt^2}\mathbf{R} = -\frac{\mu_\odot}{R^3}\mathbf{R} + \sum_{k=1}^{N_{ncb}} \mathbf{P}_k \tag{2.2.27}$$

Let us first define the current HIF. The origin is the Sun's center of mass. The three spatial axes are obtained from the axes of the International Celestial Reference System (ICRS) counter-clockwise rotated about the ICRS X-axis by the eclectic obliquity at J2000 [12, 21]. TDB matches the JPL's ephemeris time $T_{eph}$ for any practical purposes; thus, for instance, we can use the JPL ephemeris file DE430 for calculating the (classical) planetary gravitational perturbations $P_k$ $(k = 1, \ldots, N_{ncb})$ (for simplicity, we use the mentioned ephemeris files even though our equations pertain to classical dynamics), where $N_{ncb}$ is the number of non-central bodies considered in the problem.

Considering the probe as a SPS the equations becomes:

$$\begin{aligned}
\frac{d^2}{dt^2}\mathbf{R} + \frac{\mu_\odot}{R^3}\mathbf{R} &= \frac{\mu_\odot}{R^2}\Xi^{HIF}_{HOF}\mathbf{L}^{HOF} + \sum_{k=1}^{N_{ncb}} \mathbf{P}_k \\
&= \frac{\mu_\odot}{R^2}\left(\mathcal{L}_r\mathbf{r} + \mathcal{L}_t\mathbf{h}\times\mathbf{r} + \mathcal{L}_h\mathbf{h}\right) + \sum_{k=1}^{N_{ncb}} \mathbf{P}_k \qquad (2.2.28)\\
\mathcal{L}_r &\geq 0
\end{aligned}$$

Note that there is no differential equation for sailcraft mass because SPS is strictly propellant-less. If there were some mass jettisoning, this may be dealt with by a step function. For the current mission concept, however, no mass change is considered even from the attitude control viewpoint.

The three parameters in Eq. (2.2.28) are the components of the lightness vector $\mathbf{L}^{HOF}$, or simply $\mathbf{L}$, the expression of which is given in Ref. [[12], Eqn.(6.136)] for a sufficiently flat sail. The mentioned equation in Ref. [12] holds even for any sail surface element considered as flat. Thus, for instance, the effect on thrust from a curved sail can be computed by integration over the sail's surface region. $\mathbf{L}$ is resolved in the ORS of the sailcraft because it is in such frame that the acceleration measurements are made. Note that the ORS is coincident to the heliocentric orbital frame (HOF) when the primary body is the Sun. $\Xi^{HIF}_{HOF}$ is the rotation matrix from HOF to HIF. Eq. (2.2.28) contain two types of perturbations to the (restricted) two-body problem: (A) the usual planetary perturbations (e.g. Ref. [22]), and (B) the solar-photon propulsion. Motion via SPS, however, cannot be derived from a potential, in general; in addition, it does not represent a mere perturbation to the central gravitational field inasmuch as, with the evolution of technology, the solar radiation pressure acceleration on the sailcraft may become of the same order of magnitude of the central field, or not so much less as the current problem shows. In Eq. (2.2.28) $\mathbf{r} \equiv \mathbf{R}/R$ and $\mathbf{h} \equiv R \times V / |R \times V|$. In the current problem, h makes a small angle with the Z-axis of HIF.

The importance of the components $\mathcal{L}_r$, $\mathcal{L}_t$, and $\mathcal{L}_h$ of $\mathbf{L}$, here called the radial (lightness) number, the transversal number, and the normal number, respectively, relies on the expressions of the orbital energy, the energy rate, the orbital angular momentum rate, and the trajectory curvature and torsion. From Ref. [12], we report only those of interest here by ignoring (for the moment) the planetary perturbations:

$$\begin{gathered} E=\frac{1}{2}V^2-\frac{\mu_\odot}{R}\left(1-\mathcal{L}_r\right), \quad H=RV\sin\varphi \\ \frac{dH}{dt}=\mathcal{L}_t\frac{\mu_\odot}{R}, \quad \frac{dE}{dt}=\frac{H}{R^2}\frac{dH}{dt}+\frac{\mu_\odot}{R}\frac{d\mathcal{L}_r}{dt}=\frac{\mu_\odot}{R}\left(\frac{H}{R^2}\mathcal{L}_t+\frac{d\mathcal{L}_r}{dt}\right) \end{gathered} \tag{2.2.29}$$

In Eq. (2.2.29), $V$ denotes the sailcraft speed, i.e. $V=|V|$, $E$ is the sailcraft's orbital energy, and $\vartheta$ is the angle from $R$ to $V$, in the order. Out of the many properties that Eq. (2.2.29) describe, we focus on those ones useful in the current SEMB-sync problem. First, the orbital energy depends on the radial number; second, $E$ is no longer a constant of motion unless the equality

$$\frac{H}{R^2}\mathcal{L}_t+\frac{d\mathcal{L}_r}{dt}=0 \tag{2.2.30}$$

holds identically in a finite interval of time. Third, even by keeping the sail attitude constant in HOF (in this context, some useful references are [23–25]), but with $\mathcal{L}_t\neq 0$, sailcraft energy changes over time and, consequently, velocity varies. More explicitly, the along-track component of the total acceleration changes as

$$\mathbf{V}\frac{d}{dt}\mathbf{V}=V\frac{dV}{dt}=V\frac{\mu_\odot}{R^2}\left(-\cos\left(\varphi\right)\left(1-\mathcal{L}_r\right)+\sin\left(\varphi\right)\mathcal{L}_t\right) \tag{2.2.31}$$

With regard to the orbital angular momentum, say, $\mathbf{H}$, we report from Ref. [12] again

$$\frac{d}{dt}\mathbf{H}=\frac{\mu_\odot}{R}\left(\mathcal{L}_t\mathbf{h}-\mathcal{L}_t\mathbf{h}\times\mathbf{r}\right) \tag{2.2.32}$$

that depends on both the transversal and normal numbers. Though not restricted to solar sailing, one should note that the overall change of $\mathbf{H}$ is proportional to the potential energy, and a positive value of the normal number induces a rotation of the vehicle's orbit plane about the axis $\mathbf{r}\times\mathbf{h}$. If one likes to change only the magnitude of the angular momentum, then the normal number should vanish; since this cannot be done exactly in practice, very small time-varying $\mathcal{L}_n$ values may appear as noise.

## 2.3 Optimization

Spacecraft trajectory optimization has a long and interesting history that affects several areas of astrodynamics, including the design of low-energy transfers–either ballistic or low-thrust enabled–, spacecraft formation flight, and planetary defense. A lot of scientific publications on optimization regards the more different arguments: low energy transfer using the invariant manifold in the three body problem, ballistic [26] or using a low thrust [27]; to maintain a formation flight for a fleet of satellites [28]; to analyse mission to deflect hazardous asteroids [29, 30].

The problem could be simply described as the determination of a probe's trajectory that satisfy some constrains and at the same time minimize a cost quantity. The most common cost quantity is the propellant used by the propulsion subsystem, because that means to maximize the payload mass. Using low thrust engine, the cost quantity becomes the transfer time with the same meaning.

Generally, an optimization is a very high complexity continuous problem. The complexities are generally attributed to: a) the non-linear dynamic system and by the fact that the trajectory almost the times contains some discontinuities (like eclipses or impulsive variation of velocity due by a thruster); b) the possibility that the initial and final condition are partially known, for example the rendezvous with a planet used to do a swing-by; c) the dependence by forces like the perturbation due by other planets during an interplanetary transfer.

Using a chemical propulsion system, the time of burn for a deep space manoeuvre could be considered as an instant (impulsive) compared to the entire trajectory time. The continuous control of a low thrust engine is qualitatively different from the impulsive case. Its time continuity must be modelled and integrated. As example we could consider the electrical power provided by a solar cells array or the thrust due by a solar sail, it is required to take in account the distance between the probe and the Sun.

The mathematical formulation for the optimal problem consists to consider the first order differential equations of the dynamical system

$$\dot{x} = f\left(x\left(t\right), u\left(t\right), t\right) \tag{2.3.1}$$

where the independent variable is the time $t$ and it is considered in the interval $[t_0, t_f]$. $x\left(t\right)$, $u\left(t\right)$ and $f$ are the state vector, the control vector and the algebraic functions vector, respectively.

The problem's optimization consists on the determination of the state and control in function of the time to satisfy the initial and final condition and at the same time minimize a cost function $J$:

$$J = \phi\left(x\left(t_f\right), t_f\right) + \int_{t_0}^{t_f} L\left(x\left(t\right), u\left(t\right), t\right) dt \tag{2.3.2}$$

where it is possible to identify two contributions: the first one that depends by the state at the final time; a second one that depends by state and control in the entire interval time.

The necessary conditions to obtain the optimum in every space mission could be obtained using the calculation of variations. Unfortunately the resulting solution for the system of equations and the boundary conditions could be very difficult or in same case impossible to be obtained.

The highest percent of mission analysts and researchers today prefer to use numerical optimization. The optimization methods for the optimum continuous control are generally divided in three classes:

- **indirect methods**
  usually, they use an analytically approach to obtain the equation due by the calculation of variations [31]. This requires the definition of the co-state that has the same dimension of the state and this means that the dynamics' size immediately doubles. The problem has a limited number of variable but an higher difficulty to insert some constrains. The absence of physical meaning of co-state increase also the understanding problem and the setting of weights for the J functional.
- **heuristic methods**
  they are a really new algorithm branch for numerics. The particle swarm [32] or genetic algorithm [33] are used to explore the J function solution hyperspace. For both algorithms the particles or genes evolve at every iteration, for the first one they move in the domain with a velocity, in the second one they combine their self in to new entities and a Darwin selection is applied.
- **direct methods**
  they are characterized by a huge amount of variables that the optimizer has the charge to manipulate. These methods have the disadvantage of to use a lot of variables, but at the same time the oxymoron constrains. One of them is the collocation method [34]

The space missions analysed in this thesis are optimized using this last method. Changing the gravitational dynamic model, all the optimized trajectories are obtained using SNOPT [35]. We assign the optimization state vector that consists commonly into attitude angles and the length of the thrusting arcs. Sometime instead of the euler angles we used the component of the sailcraft surface normal, that permit a faster convergence.

# 3

# Low Thrust Trajectory Optimization

In this chapter we present three space mission using different reflection models for the solar sail. Firstly, an Alpha Centauri mission is presented with a perfect reflection model. I would like to empathize the presence of two emitting body in an elliptic restricted three body problem. Secondly the problem of early warning for coronal mass ejection is introduced and a mission that uses the solar photon sailing to virtually move the equilibrium point L1 closer to the Sun is presented. An overview of the synchronism problem is discussed and a detailed reflection model is used in a full ephemeris N-body problem propagation. Finally, a preliminary numerical analysis varying the sail-craft performance is presented. The missions are a circular-circular planar orbital change from Earth to Mercury orbit and from Earth to Mars orbit.

## 3.1 Alpha Centauri Tour analysis

The binary star system of Alpha Centauri A/B has scientific importance and its exploration could give a great opportunity to increase knowledge about our solar system. The analysis of chemical composition and luminosity of these stars could be used to understand the Sun better [36]. Observing the orbits of star dust particles could improve knowledge about planetary formation and their accretion discs [37]. Furthermore, the high metallic content of both stars suggests the existence of stellar discs from which planets may originate [38–41]. Thus, the rank of A/B as the first target in future interstellar exploration is very high. Though today the funding of a specific interstellar mission is premature, the time, however, has come for suggesting a number of scientific goals, various mission requirements and necessary technology advances [9].

It had been envisaged the following scenario: by the end of the $21^{st}$ century, a two-stage rocket-propulsion starship will be funded for the first mission to the Alpha-Centauri star system. Both stages are assumed to be powered by thermonuclear engines, presumably an advanced version of the Project Daedalus of the British Interplanetary Society [42], which aimed at exploring the Barnard star (at that time Barnard star had been given an exploration rank higher than Alpha Centauri.). The second stage decelerates down to a certain distance, say, $R_{inj}$ from the A/B barycentre with a speed, say, $V_{inj}$. Here $R_{inj}$ is supposed to be a few semi-major axes of the relative orbit of A/B. $V_{inj}$ is sufficiently low to be able to inject the starprobes onto an orbit about either A or B, but sufficiently high to allow the starship's second stage to reach the gravitational lens region of the A/B system in a few years. There, the communication station can be released and installed. This station is supposed to receive data from the probes and relay them to the solar system, and vice versa. The fully-automated probes represent the main payload of the starship, and will be designed to explore the stellar particle environments by utilising the irradiances from A and B and their stellar winds and to observe the A/B planets. Thus, they move in the *full* gravitational and photon fields of both stars.

### 3.1.1 Alpha Centauri System

The Alpha Centauri system ($\alpha$Cen) is located at 4.37 light years from the Sun and is composed of three stars: Alpha Centauri A ($\alpha$CenA), Alpha Centauri B ($\alpha$CenB) and Alpha Centauri C, better known as Proxima Centauri, far away from the previous two. The most massive stars are $\alpha$CenA and $\alpha$CenB, which form a binary system; their relative elliptic orbits exhibit a semimajor axis $a = 23.4$ AU and eccentricity $e = 0.5179$. Table 3.1.1 reports the principal characteristics of $\alpha$CenA and $\alpha$CenB with respect to the Sun [43, 44].

**Table 3.1.1:** $\alpha$CenA and $\alpha$CenB principal characteristics

| | Mass $M_{Sun}$ | Radius $R_{Sun}$ | Luminosity $L_{Sun}$ | Temperature $K$ |
|---|---|---|---|---|
| $\alpha$CenA | 1.100 | 1.227 | 1.519 | 5790 |
| $\alpha$CenB | 0.907 | 0.865 | 0.500 | 5260 |

Proxima Centauri is located about 15'000 AU from the $\alpha$Cen barycentre, and its mass is estimated at 0.123 $M_{Sun}$ (Beech, 2011). Due to the lower mass and the large distance from the binary star system, Proxima is assumed to have a negligible gravitational influence on the other two stars. Therefore, it is neglected in studying the motion of a sailcraft about the other two. With respect to the International Celestial Reference Frame (mean ecliptic at J2000), the position of the barycentre of $\alpha$Cen system is identified by two angles: ecliptic longitude $\lambda = 188.37$ deg and the ecliptic latitude $\beta = 68.18$ deg [44]. In addition, Alpha Centauri moves respect to the solar system with radial speed $V_R = 21.6$ km/s and with angular speeds $\dot{\lambda} = 3.678$ arcs/year and $\dot{\beta} = 0.481$ arcs/year [45]. For a mission to $\alpha$Cen, due to the long transfer time, it is necessary to know how the star system vector position and orbital plane orientation change with time. To this aim, let us define an inertial reference system called Barycentric Stellar Reference System (BSRS) $(\hat{\boldsymbol{e}}; \hat{\boldsymbol{h}} \times \hat{\boldsymbol{e}}; \hat{\boldsymbol{h}})$: its origin coincides with the $\alpha$Cen barycentre, the x -axis coincides with the eccentricity vector e of the relative ellipse of A/B; the z axis coincides with the orbital angular momentum vector h of the $\alpha$Cen system and the third axis completes the right-hand triad. Fig. 3.1.1 shows the A/B orbital plane with respect to the mean ecliptic at J2000 [46].

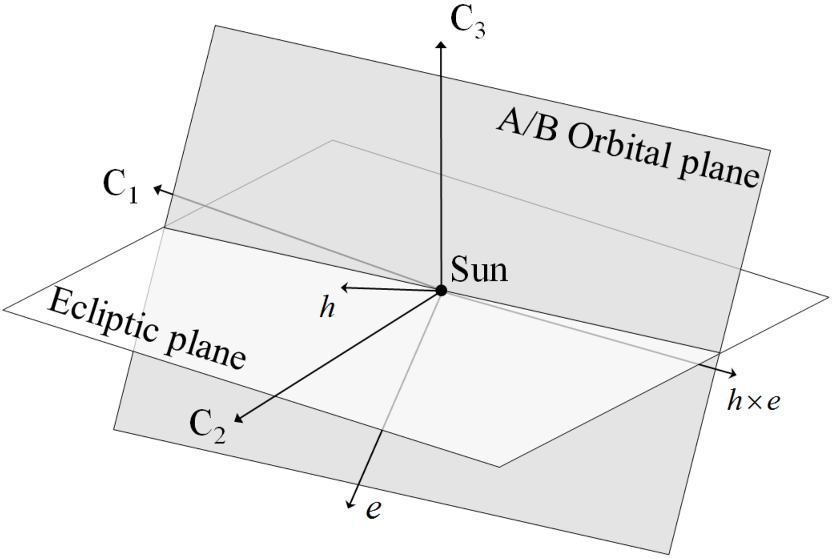

**Figure 3.1.1:** A/B orbital plane with respect to the mean ecliptic at J2000.

The Sun's direction in BSRS can be specified by two angles: the longitude $\varepsilon_{Sun}$ and the latitude $\chi_{Sun}$ (Fig. 3.1.2). With the previous radial and angular velocities [45] the latitude and longitude values will decrease from $\varepsilon_{Sun} = 243.37$ deg to $\varepsilon_{Sun} = 243.29$ deg and from $\chi_{Sun} = 4.39$ deg to $\chi_{Sun} = 4.18$ deg in the next 200 years. Due to the mentioned radial speed

($V_R$), the accumulated shift of 5 day-lights, at the most, is neglected.

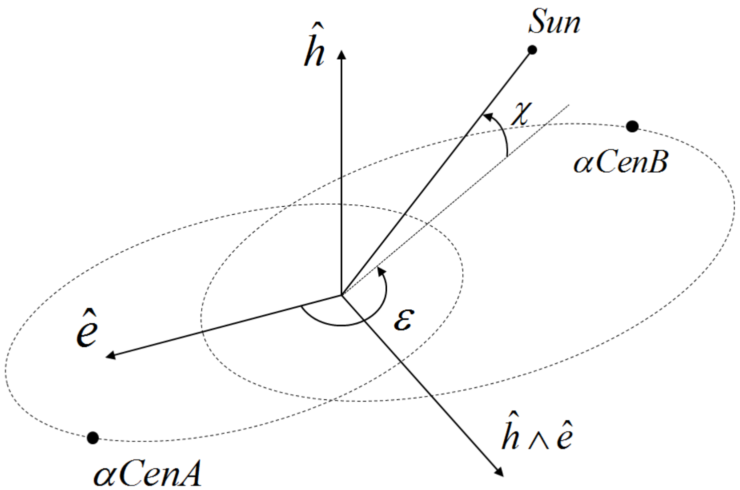

**Figure 3.1.2:** Sun direction in BSRS.

### 3.1.2 Equation of motion

In addition to the BSRS, another two reference systems are introduced to study the sailcraft motion. The Barycentric Rotating Reference System (BRRS) is defined as having its origin coincident with the barycentre of A/B, the x-axis pointing to Alpha Centauri B, the z-axis is oriented as the orbital angular momentum of A/B, and the y-axis completes the right-hand triad. When we adopt the instantaneous distance between A and B as the unit length, BRRS results in the reference system where both stars are fixed at any time. We call it the Barycentric Fixed Reference System (BFRS). The sailcraft motion in the $\alpha$Cen system can be studied by using the elliptical restricted three-body problem (Sec. 2.2.2) in which the sail is simultaneously irradiated by the light of A and B.

The lightness vector formalism is used to express the thrust acceleration [12]. Respect the definition in Eq. (2.1.8), the components of the lightness vector (one for A and one for B) are:

$$\mathbf{L}_j = \mathcal{L}_{max_j} \cos^2 \gamma_j \cos^2 \varphi_j \begin{pmatrix} \cos \gamma_j \cos \varphi_j \\ \cos \gamma_j \sin \varphi_j \\ \sin \gamma_j \end{pmatrix} \begin{pmatrix} \hat{r_j} \\ \hat{\vartheta_j} \\ \hat{h_j} \end{pmatrix}, j = A, B \quad (3.1.1)$$

with:

$$\mathcal{L}_{max_B} = \frac{0.500}{0.907}\mathcal{L}_{max_{Sun}}, \mathcal{L}_{max_A} = \frac{1.519}{1.100}\mathcal{L}_{max_{Sun}} \qquad (3.1.2)$$

where $\mathcal{L}_{max_{Sun}}$ is the maximum sailcraft lightness number if we consider the Sun as the emitting body. The ratio introduced in these formulae depend on luminosity and mass of the considered star and is modified accordingly to the values of Table 3.1.1.

### 3.1.3 Numerical simulations

An exploration mission of the $\alpha$Cen system can be divided into four parts. The first one is the *capture phase* from the interstellar trajectory to a close orbit about the brightest star $\alpha$CenA. After the capture, the goal is to study the physical characteristics of $\alpha$CenA. To this aim, the sailcraft orbit inclination is first increased to reach 90 deg and then reduced to return to zero degrees. The third part regards the study of the transfer trajectory from the orbit about $\alpha$CenA to an orbit about $\alpha$CenB. Finally, in the last phase, the inclination of the sailcraft orbit is changed from zero to 90 deg to study the physical characteristics of $\alpha$CenB. Because stellar-photon sailing is propellantless, the cost index to be minimised is the transfer time for each phase of the mission and, due to its stability and facility to implement constraints, a Direct Method approach is used. Each phase of the mission is divided into an optimum number of arcs of trajectory, and each arc is associated with three variables: the temporal length of the arc and two sailcraft attitude angles. The sailcraft attitude angles refer to the closest star and, to reduce the numerical complexity of the problem, are supposed constant in the same arc with respect to the ORS. The optimum values of the attitude angles, the temporal length and the number of the arcs are found by using the SNOPT optimiser [35]. The maximum sailcraft lightness number used for the capture phase is $\mathcal{L}_{max_{Sun}} = 0.6$, while for the other phases it is $\mathcal{L}_{max_{Sun}} = 0.4$ (the sailcraft is supposed to be designed to vary the sail area according to mission requirements). $\mathcal{L}_{max_{Sun}} = 0.6$ has been selected because for lower values the capture manoeuvre is difficult to obtain, while for other phases, the maximum sailcraft lightness number has been reduced to limit the disturbance force produced by the other star, but to avoid a too long transfer time it has been decided not to use a lightness number lower than 0.4. Finally, for every phase of the mission, the optimum number of arcs is selected in a range of values defined using a preliminary numerical analysis.

Capture phase

The capture problem is sensitive to the approaching parameter and the choice of the initial values play a key role in the trajectory performance (Hyeraci and Topputo, 2010, 2013; Circi, 2012). As mentioned before, in BSRS the direction of the Sun is determined by longitude $\epsilon_{Sun}$ and latitude $\chi_{Sun}$, where the latitude is only 4,18 deg. Hence the out-of-plane latitude is a small angle, the thermonuclear engine, necessary for the interstellar transfer, could reduce it to zero, obtaining a coplanar motion with A/B ($\chi_{Sun} = 0$). Alpha Centauri A's heliosphere is similar to the Sun's heliosphere and therefore a possible value for the release distance $d$, point from which the trajectory leaves the interstellar phase and is considered about the barycentre of the stellar system, could be chosen at $d = 200AU$ (Steinolfson and Gurnett, 1995). Another important parameter is the impact parameter $B$. In order to obtain a stellar pressure force that allows the capture manoeuvre efficiently, the values of $B = 4AU$ is selected. Because the luminosity of $\alpha$CenA is 1.5 times bigger than that of the Sun, the release velocity at distance d to obtain an effective capture results in the range from 60 km/s to 80 km/s. Finally, the relative position of stars with respect to the release point d is defined by the entry angle d (the angle between the Sun-$\alpha$Cen system centre of mass line and the $\alpha$CenA - $\alpha$CenB line). The value of d is an output of the parametrical optimisation problem. The release condition values are summarised in Tab. 3.1.2. From the release point we reduce the velocity of the sailcraft to achieve a circular orbit with radius of $\sqrt{1.5}$ AU. This distance has been chosen in order to receive the same irradiance as received at 1 AU from the Sun. To reduce the velocity and obtain a successful capture, a close approach with $\alpha$CenA is necessary. In heliocentric trajectory to avoid thermal problems the minimum distance from the Sun is equal to 0.2 AU (Dandouras et al., 2004). Considering the physical properties of aCenA we obtain 0.3 AU as a safety distance value. After the first pericentre passage the manoeuvre is optimised with an angular momentum reversal strategy. The capture phase is divided into five arcs (optimum number in the range from 4 to 7), needs around 16.799 years to be completed, and the optimum value for the entry angle is $\delta = 25^o 54' 34.81''$. Fig. 3.1.3 shows the capure trajectory

**Table 3.1.2:** Release condition values

| $B$ (AU) | $d$ (AU) | $\chi$ (deg) | $\left\lvert \vec{V_\infty} \right\rvert$ (km/s) |
|---|---|---|---|
| 4 | 200 | 0 | 60 |

in BFRS. The dot-dashed line represents the osculating orbit at the end of the capture phase while the bars represent the sail attitude every 100 days.

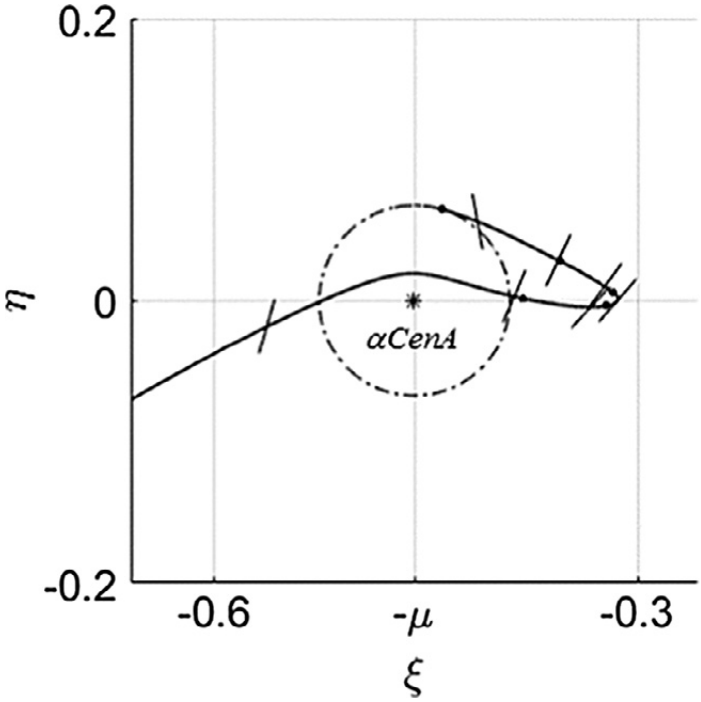

**Figure 3.1.3:** Capture trajectory about $\alpha$CenA in BFRS.

Tab. 3.1.3 shows the attitude angles magnitude in ORS and the arc duration for each of the five arcs (because the motion is in the plane the out of plane attitude angle is null). The first arc is longer than the others, 15.364 years, contrariwise the duration of the other arcs are around 0.36 years. At the end of this phase, the final circular orbit at $\sqrt{1.5}$ AU is achieved.

**Table 3.1.3:** Arc duration and attitude angles in ORS during the capture trajectory

| Arc length (years) | $\varphi$ (deg) |
|---|---|
| 15.364 | 26.15 |
| 0.359 | 43.85 |
| 0.347 | 61.45 |
| 0.360 | 41.13 |
| 0.368 | 19.87 |

Polar orbit about Alpha Centauri A

In order to study the physical properties of $\alpha$CenA as function of stellar latitude, a transfer trajectory to a circular polar orbit (with the same radius as the initial one), and the return to the equatorial plane has been optimised (minimum time). The transfer trajectory has been divided into 13 arcs (optimum number in the range from 5 to 18). The polar orbit is achieved in 1.612 years (Fig. 3.1.4), while the complete phase including the return to the equatorial plane, in 3.310 years. Fig. 3.1.5 shows the

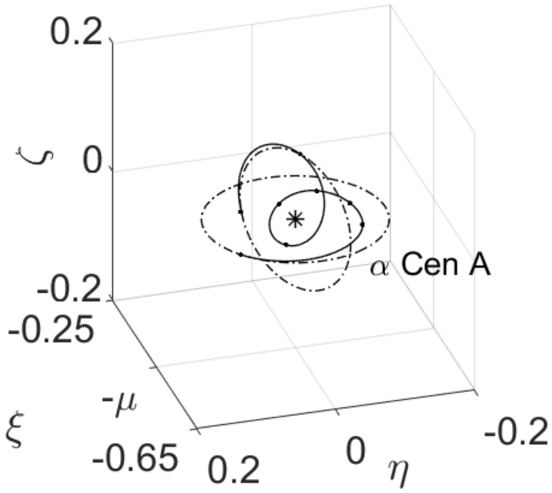

**Figure 3.1.4:** Polar circular orbit about $\alpha$CenA in BFRS.

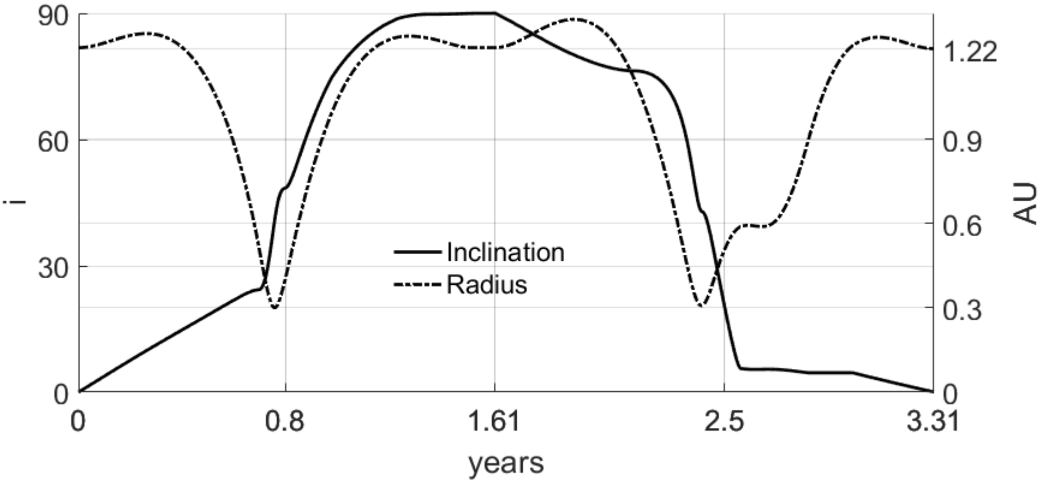

**Figure 3.1.5:** The inclination variation about $\alpha$CenA.

inclination during the manoeuvre. The optimal trajectory shows a reduction of the distance from $\alpha$CenA, which allows the use of more energy due to the star luminosity and it is possible to identify the highest inclination variation when the distance to the star is minimal at around 0.761 years. Tab. 3.1.4 shows the optimal temporal length and the attitude angles values in ORS during each of the 13 arcs. In this case we have in plane ($\varphi$) and out of plane ($\gamma$) angles.

**Table 3.1.4:** Attitude angles in ORS during the out of plane trajectory about $\alpha$CenA

| Arc length (years) | $\varphi$ (deg) | $\delta$ (deg) |
|---|---|---|
| 0.697 | -37.32 | -33.87 |
| 0.101 | -5.36 | 34.42 |
| 0.179 | 7.64 | -28.52 |
| 0.261 | 24.98 | -26.45 |
| 0.113 | 32.45 | -19.13 |
| 0.167 | 45.41 | 2.57 |
| 0.091 | -78.64 | 73.86 |
| 0.697 | -34.68 | -21.20 |
| 0.101 | -5.88 | 28.07 |
| 0.179 | -2.74 | -28.25 |
| 0.261 | 13.48 | 6.04 |
| 0.113 | 89.99 | -24.37 |
| 0.167 | 43.75 | 9.88 |

Transfer trajectory from $\alpha$CenA to $\alpha$CenB

As mentioned before, the selected circular orbit about $\alpha$CenA has a radius of $\sqrt{1.5}$ AU in order to receive the same irradiance as received at 1 AU from the Sun. For the same reason the target circular orbit about $\alpha$CenB has been chosen with a radius of $\sqrt{0.5}$ AU. In addition, this distance allows the observation of the Earth size planet orbiting about $\alpha$CenB [39]. In this phase a minimum transfer time trajectory from $\alpha$CenA to $\alpha$CenB is studied. The trajectory is divided into 11 arcs (optimum number in the range from 5 to 16) and the transfer trajectory is completed in 7.564 years. In Fig. 3.1.6 the meaning of dot-dashed lines and bars are the same as Fig. 3.1.3. Tab. 3.1.5 shows the attitude angles in ORS during each of the eleven arcs. In this case their values are in the range of $[-84^o; +53^o]$ and are necessary only in plane angle (planar motion, $\gamma = 0$).

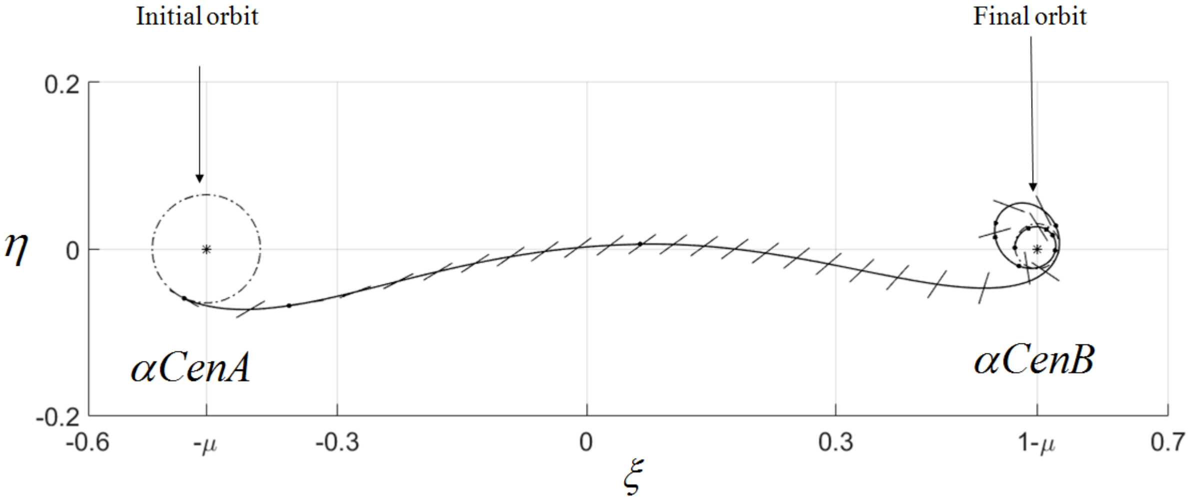

**Figure 3.1.6:** Transfer trajectory from $\alpha$CenA to $\alpha$CenB in BFRS.

**Table 3.1.5:** Attitude angles in ORS during the transfer trajectory from $\alpha$CenA to $\alpha$CenB.

| Arc length (years) | $\varphi$ (deg) |
|---|---|
| 0.454 | 5.91 |
| 2.544 | 13.59 |
| 3.206 | -40.63 |
| 0.567 | -84.20 |
| 0.110 | -84.76 |
| 0.207 | -84.48 |
| 0.163 | -37.54 |
| 0.066 | -68.99 |
| 0.038 | -25.89 |
| 0.088 | 33.84 |
| 0.116 | 53.71 |

Polar orbit about Alpha Centauri B

In this section the minimum transfer time trajectory from an equatorial to a polar orbit about $\alpha$CenB is studied. The trajectory is divided into 13 arcs (optimum number in the range from 3 to 15) and the total transfer time is 4.504 years. With respect to $\alpha$CenA's case, the optimum manoeuvre does not consist in decreasing the distance from the emitting body because of the low flux of power. In fact, to obtain a good result in terms of transfer time, it is necessary to arrive very close to the star where thermal problems could not be negligible. The best strategy consists in maintaining fixed the osculating semi-axis and eccentricity and varying only the inclination (Fig. 3.1.7) [47, 48]. Tab. 3.1.6 shows the attitude

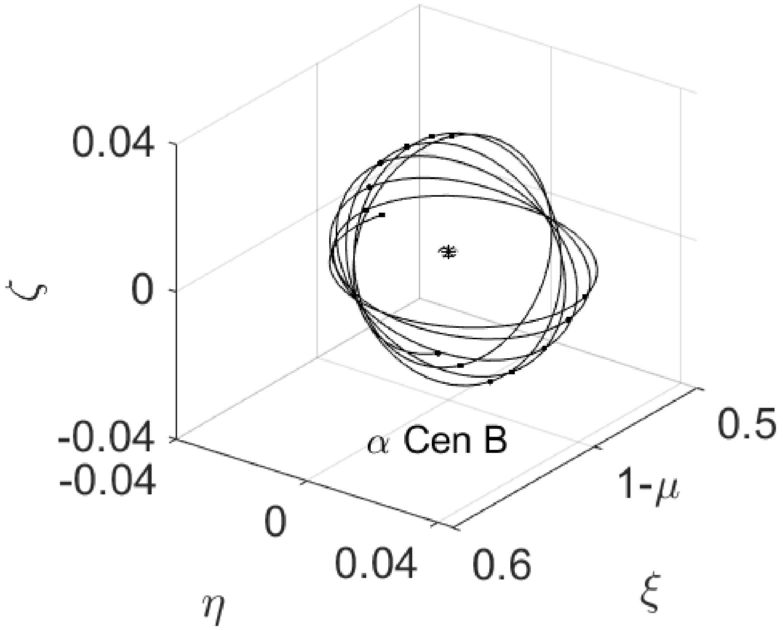

**Figure 3.1.7:** Changing inclination manoeuvre about $\alpha$CenB

angles in ORS during each of the thirteen arcs. In this case we have in plane ($\varphi$) and out of plane ($\gamma$) angles. Their values are in the range of $[-68^o; +62^o]$ and the arcs have comparable temporal lengths.

### 3.1.4 Zero Velocity Curves analysis

An analysis of this exploration mission is possible in terms of ZVC (Sec. 2.2.2). In fact, for the elliptical three-body problem the geometry of ZVC is not constant and it changes during the trajectory [49, 50]. Fig. 3.1.8 highlights four instants during the capture manoeuvre. The subfigure (a) shows the ZVC completely open before the closest approach to aCenA, the energy is still too high. The second subfigure (b) shows the energy level after the nearest passage: the capture is completed. The third subfigure (c), emphasise the momentum reversal instant while the last subfigure (d) shows the energy at the target orbit. Similarly Fig. 3.1.9 shows the ZVC in four different instants during the transfer trajectory fromaCenA to aCenB. At the beginning of the transfer the ZVC are still closed (a, b). In the next

**Table 3.1.6:** Attitude angles in ORS during the out of plane trajectory about $\alpha$CenA

| Arc length (years) | $\varphi$ (deg) | $\delta$ (deg) |
|---:|---:|---:|
| 0.399 | -4.54 | -67.96 |
| 0.292 | -4.19 | 62.24 |
| 0.361 | 9.14 | -66.76 |
| 0.321 | -0.53 | 50.47 |
| 0.365 | 1.68 | -55.64 |
| 0.341 | -3.63 | 44.06 |
| 0.347 | 4.63 | -47.17 |
| 0.351 | -2.27 | 48.95 |
| 0.349 | 3.65 | -48.82 |
| 0.380 | -1.01 | 42.92 |
| 0.319 | 0.50 | -58.06 |
| 0.354 | 3.90 | 53.03 |
| 0.321 | -9.91 | -60.86 |

subfigures (c, d), the curves are open and the sailcraft has enough energy to reach the other star. In the last subfigures (e, f), the transfer manoeuvre to achieve a closed orbit about aCenB is accomplished.

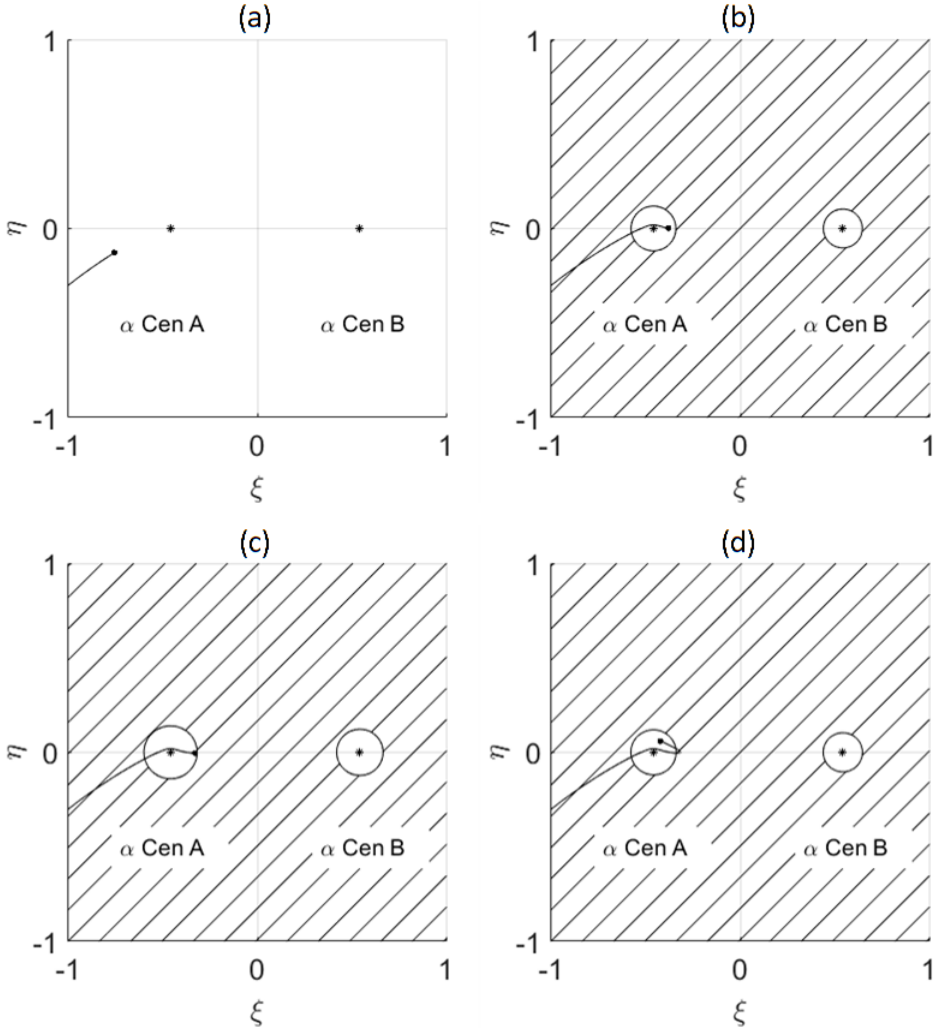

**Figure 3.1.8:** ZVC during the capture manoeuvre about $\alpha$CenA

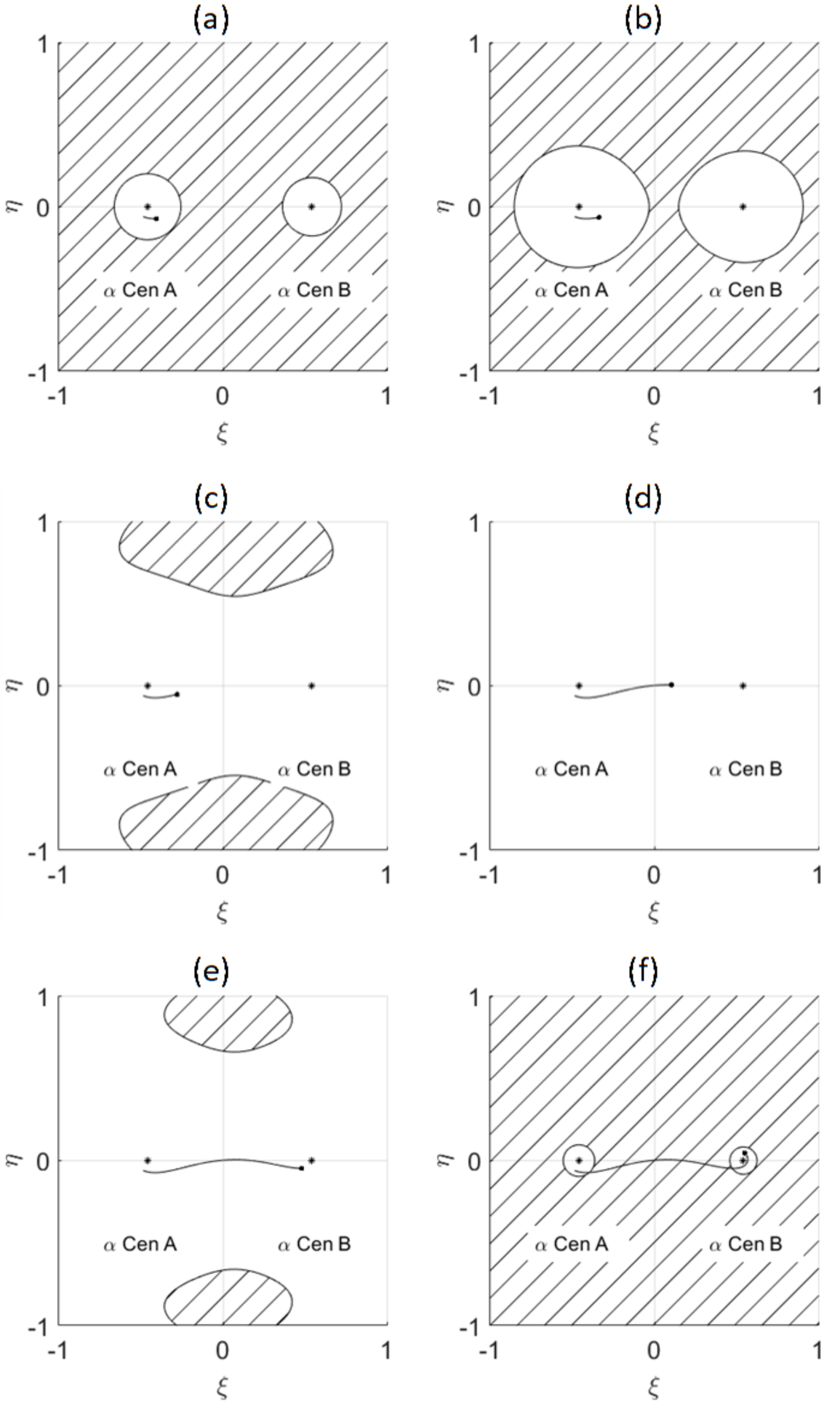

**Figure 3.1.9:** ZVC during the transfer trajectory from $\alpha$CenA to $\alpha$CenB

## 3.2 Early Warning Mission

The propellantless in-space propulsion mode, known as the solarphoton sailing (SPS) [11–13, 17, 51–53], could help the countries even in serious problems owing to unpredictable events in space weather. One of such event type is the Coronal Mass Ejection (CME) from the solar corona. A CME involves a large fraction of the solar corona; normally, the ejected plasma reaches the Earth neighborhood after a few days. In rare cases, the plasma particles are so fast to reach the magnetosphere in less than one day. Also, the interaction of the main components of the solar wind, i.e. the so-called slow wind and fast streams, may bring forth the conditions for geomagnetic storms (GSs) lasting times longer than those related to CMEs, usually giving the magnetosphere more energy with respect to the energy deposited by a CME. A GS is a significant perturbation of the magnetosphere of the Earth. Such a storm takes place if there is significant energy exchange between the solar wind and the space environment around the Earth. The plasma in this environment is then changed strongly. The solar-wind conditions allowing such an interaction consist of (1) wind's fast particles (i.e. with high dynamical pressure), and mainly (2) when the direction of the wind's magnetic field is opposite to the Earth's magnetic field at the magnetosphere dayside. Through the complex phenomenon of the magnetic reconnection [54–56], the Earth's magnetic field lines become connected to the wind field lines; thus, the dayside magnetosphere opens up, and an intense transfer of energy can take place from the solar wind to the magnetosphere. In particular, there is a remarkable penetration of the charged solar-wind particles into the ionosphere whereupon the inside electric currents change notably.

Spacecraft ACE (NASA) satisfies both synchrony conditions, but it guarantees a warning time of about 30 min for (typical) fast streams of 800 km/s. As a point of fact, ACE moves about the L1 point of the gravitational Sun-Earth system (Sec. 2.2.2), i.e. 1.5 million kilometres sun-wards from EMB. A sailcraft can be designed to operate around L1 or L2 for not spending propellant [57], and may be moved between halo orbits of different Sun-planet systems [58]. The present chapter describes a research into the early warning of CME induced solar storm via an advanced sailcraft. Conceptually, an early-warning sailcraft can efficiently satisfy its aim if it is (i) on a heliocentric orbit internal to the orbit of the Earth-Moon barycentre (EMB), and (ii) on the segment Sun-EMB for all operational time. In practice, condition (ii) can be met only within some assigned tolerance, namely, in some given box about the nominal station point. The shape of this box may be modified according to mission-dependent communication constraints; this situation will be analysed in detail in future works.

Around L1, a space vehicle has a period very close to 1 year. Nevertheless, if one wants a 1-year low-eccentricity orbits with (a) a semi-major axis remarkably less than 1 AU, and (b) no propellant for achieving and controlling the operational orbit, then the only known way is to have recourse to a sailcraft with a sufficiently high lightness number [59]. The principle is simple. A sailcraft with the sail orthogonal to sunlight senses the Sun with a reduced gravitational mass depending on the lightness number of the whole sailcraft [11–13]. Later on, we will show that increasing this number causes a decrease of the sailcraft orbit semi-major axis, thus allowing longer warning time as soon as a CME-related solar plasma transient is detected.

### 3.2.1 Statement of the problem

In this Section, we describe a simple theory of the SEMB-sync problem. This research stems from the preliminary work made in Refs. [52, 59], where, in particular, the period of a sailcraft's elliptical orbit was plotted as function of the semi-major axis and the radial lightness number, denoted by $\mathcal{L}_r$, which is the radial component of the sailcraft lightness vector [12]. Here, we re-plotted the basic aspects from scratch, and we show them in Fig. 3.2.1. The key point is that a sailcraft senses the Sun as having an effective gravitational mass $\mu_{\odot}^{(eff)} = \mu_{\odot}\left(1 - \mathcal{L}_r\right)$. This gives rise to generalized Keplerian orbits if the other components vanish. If the sailcraft's lightness vector has non-zero non-radial components, then the orbital energy and/or the orbital angular momentum are no longer constants of motion [12]. To describe the main points simply, let us first suppose that the sailcraft moves on an elliptic unperturbed heliocentric orbit, with semi-major axis $a_s$ and eccentricity $e_s$, coplanar with the EMB orbit, assumed elliptic as well, with semi-major axis $a_p$ and eccentricity $e_p$. This is the first assumption of the problem. The second assumption consists of $a_s < a_p$; $e_s = e_p$. One should note that this equality does not conflict with the concept of solar effective mass mentioned above. As a point of fact, if a general Keplerian orbit has orbital energy $E$ and angular momentum $\mathbf{H}$, per unit mass both, the eccentricity is expressed by $e = \sqrt{1 + 2E\left(\left|\mathbf{H}\right| / \mu_{\odot}\right)^2}$. As both $E$ and $\left|\mathbf{H}\right|^2$ are directly proportional to $1 - \mathcal{L}_r$ [12], this equation is invariant under the transformation $\mu_{\odot} \to \mu_{\odot}\left(1 - \mathcal{L}_r\right)$, $\mathcal{L}_r > 0$; thus, the relationship $e_s = e_p$ is a valid hypothesis. The SEMB-sync problem has a few requirements. The first one is obviously $P_s = P_p$, where $P$ denotes

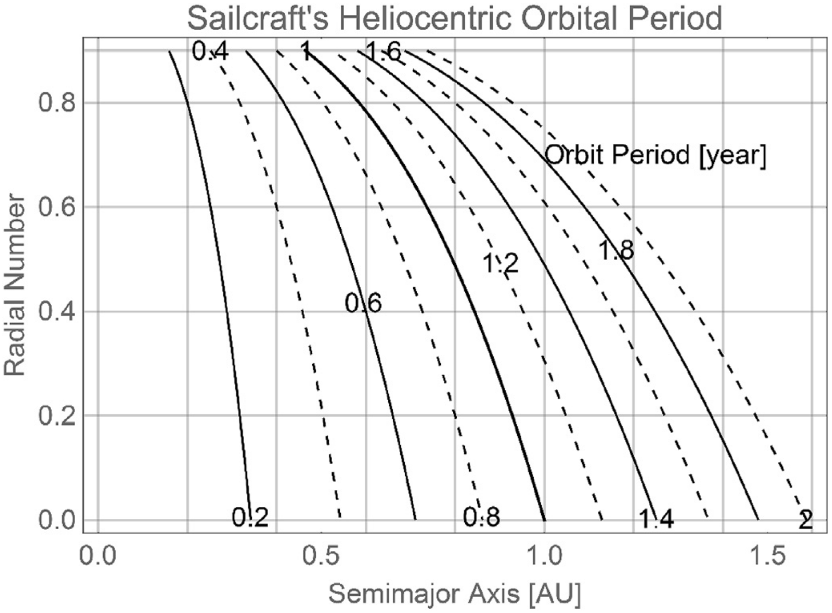

**Figure 3.2.1:** Contours of the period of a general Keplerian orbit as function of the semi-major axis (AU) and the radial lightness number

the orbital period. This entails that

$$P_s^2 = (2\pi)^2 \frac{a_s^3}{\mu_\odot (1 - \mathcal{L}_r)} = P_p^2 = (2\pi)^2 \frac{a_s^3}{\mu_\odot} \tag{3.2.1}$$

from which it is straightforward to get

$$\mathcal{L}_r = 1 - \left(\frac{a_s}{a_p}\right)^3 \tag{3.2.2}$$

Eq. (3.2.2) represents a dynamical requirement that is the major input to the sail technology, as we will show below. We have $\mathcal{L}_r > 0$ by sailing, which allows us to design a synchronous orbit with $a_s < a_p$ whereupon a significant warning time may be possible; if we achieve a technology featuring high $\mathcal{L}_r$, say, greater than 0.06 (this value corresponds to the Earth-sailcraft distance of 3.1 million kilometres, i.e. about twice the Earth-L1 distance), then may be long the warning time. Here, ‘long’ means enough to avoid serious hazards to ground, air, and space human activities.

The second mission (ideal) need is that the two true anomalies match at any time: $\theta_s(t) = \theta_p(t)$. Consequently, the difference between the

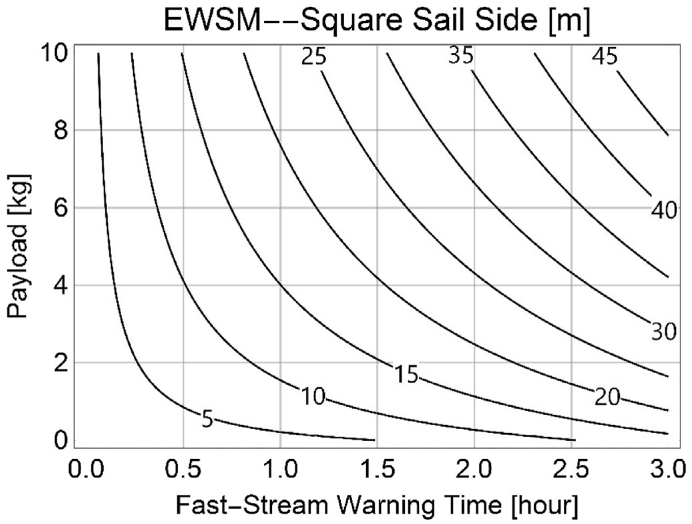

**Figure 3.2.2:** Contour lines of the sail side as function of the warning time and the gross payload mass.

EMB and sailcraft heliocentric distances is given by

$$\Delta R_{sp}\left(t\right) \equiv R_{sp}\left(t\right) - R_s\left(t\right) = \frac{1-e_p^2}{1+e_p\cos\left(\theta_p\left(t\right)\right)}\left(a_p - a_s\right) \qquad (3.2.3)$$

from which it is evident that the sailcraft-EMB distance changes (periodically) with time. As the third assumption, we suppose that the sailcraft insertion to the station takes place close to the EMB aphelion. Denoting the aphelion distance by $Q$, we set

$$Q_p - Q_s = v_{fs}\tau_{max} \qquad (3.2.4)$$

where $v_{fs}$ denotes the fast-streams speed and $\tau_{max}$ is the upper bound of the early warning time interval $\tau$. Eqs. (3.2.2) and (3.2.3), (evaluated first at $\theta_p = \pi$ and then at $\theta_p = 0$),and Eq. (3.2.4) give

$$a_s = a_p - \frac{v_{fs}\tau_{max}}{1+e_p} \qquad (3.2.5a)$$

$$\mathcal{L}_r = 1 - \left(1 - \frac{v_{fs}\tau_{max}}{\left(1+e_p\right)a_p}\right)^3 \qquad (3.2.5b)$$

$$\frac{1-e_p}{1+e_p} \leq \tau \leq \tau_{max} \qquad (3.2.5c)$$

**Remark-1**. Normally, one would need a long warning time, namely, putting as much a distance as possible between Earth and storm detector.

However, since the more internal a usual Keplerian orbit is, the shorter is its period, one needs higher value of Lr to "reduce" the mass of the Sun and increase the sailcraft period. Eq. (3.2.5b) tells us how much the lightness number must be high in order to locate the sailcraft sun-ward at distance $v_{fs}\tau_{max}$ from EMB. As the sailcraft-EMB distance cannot be constant during $P_p$, we have actually a range of allowed warning time, i.e. just that expressed in the third line of Eq. (3.2.5c). In practice, if we take on $e_p = 0.0167$ as the reference eccentricity of the EMB orbit, the lower bound of $\tau$ amounts to $0.967\tau_{max}$. This range is set by the warning time interval at the beginning of the operations.

Suppose that Eq. (3.2.5) may be carried into effect by a certain technological effort by the sailcraft-design country. One could wonder what increasing the warning time to $\tau_{max} + \xi$ ($\xi > 0$) would imply. To this aim, let us remind the reader one of the basic relationships of SPS [12, 17, 51, 52]:

$$\sigma\mathcal{L} - \eta\sigma_{(cr)} \tag{3.2.6}$$

where $\sigma = m/A$ denotes the sail loading of a sailcraft of mass m and sail area $A$. The thrust efficiency $\eta$ is defined as follows: suppose we have a sailcraft with a flat and perfectly-reflecting sail at rest in the heliocentric inertial frame a certain position $\mathbf{R}(t)$ (from the Sun) with the sail back-side unit vector $\hat{\boldsymbol{n}}$ parallel to $\mathbf{R}/R$; in these conditions, let a(ideal) be the sailcraft thrust (scalar) acceleration due to the solar radiation pressure. If another sailcraft at $\mathbf{R}(t + \Delta t) = \mathbf{R}(t)$, any $\Delta t$, with a real-sail (not necessarily flat, nor orthogonal to sunlight, nor at rest) undergoes the thrust (scalar) acceleration $a_{(actual)}$, then $\eta \equiv a_{(actual)}/a_{(ideal)}$in compliance with Refs. [12, 52, 60]. One should note that the actual and the ideal accelerations are measured (on-board) and computed, respectively, at the same sunlight irradiance. For the current case, the value of $\mathcal{L}$ appearing in Eq. (3.2.6) coincides with the $\mathcal{L}_r$ value written in the Eq. (3.2.5b). Using Eq. (3.2.6) twice by first inserting $\tau_{max}$ in $\mathcal{L}_r$ (with the technology expressed by $\sigma_0$) and then $\tau_{max} + \xi$ (with the technology expressed by $\sigma_1$), one gets

$$\frac{\sigma_1}{\sigma_0} = \frac{1 - \left(1 - \frac{v_{fs}\tau_{max}}{(1+e_p)a_p}\right)^3}{1 - \left(1 - \frac{v_{fs}(\tau_{max}+\xi)}{(1+e_p)a_p}\right)^3} \tag{3.2.7}$$

For example, as shown below, we will consider a max nominal warning time of $140min$ for the above-mentioned solar fast streams. We obtain from Eq. (3.2.7) the following equality if we like to get a warning time 25%

longer, i.e. $175min$:

$$\sigma_1 = 0.809\sigma_0 \tag{3.2.8}$$

The factor 0.81 is a notable technological effort also considering that one necessary to achieve $\sigma_0$.

### 3.2.2 Conjecturing a sailcraft for CME surveillance

The astrodynamical aspects of the SEMB-sync problem allow us to express the main features of the sailcraft system once a model of mass breakdown is chosen. Here, we have used the model explained in Ref. [60] using the Eqs. (6)-(8) with appropriate parameter values. Substantially, by the mentioned model adapted to the current case, one can consider the sail's reflecting layer (SRL), the related plastic support, the booms and its sail-open architecture (we have chosen a striped architecture with loading lines), the attitude control, the deployment subsystem, and the gross payload consisting mainly of the solar-storm detector (imager + proton sensor + magnetometer) and the communication system. Fig. 3.2.2 shows the result from the mass breakdown of a square-sail sailcraft via the contours lines of the sail side expressed as function of the gross payload mass and the storm warning time interval. We will use the acronym EWSM for this Early Warning sailcraft Mission concept.

Fig. 3.2.2 is particularly useful because, following a given contour (i.e. a certain sail side), increasing the warning time necessarily decreases the (gross) payload on-board the sailcraft. If one requires to increase both payload mass and warning time significantly, for instance along the left diagonal from the origin, a considerably larger sail area is required. An example of advanced sailcraft is shown in Tab. 3.2.1, which regards a SEMB-sync sailcraft orbiting sun-ward at about 4.5 times the L1-Earth distance, allowing a warning time of 140 min under fast streams. Note that, at such distance, the Earth-Moon system perturbs the sailcraft motion, but there are no halo orbits. Gross payload-mass is about a half of the whole sailcraft-mass.

The implementation of the lightness number in Eq. (3.2.5) comes not only from the use of Aluminium vapour-deposited on 2 $\mu m$ of CP1, but also from the choice of light booms, high-performance instruments and efficient communication system both in terms of bit rate, power, and mass (Incidentally, the sailcraft sail loading that we aim at achieving is very close to that one for SPS-based Earth-Mars shuttle [60]). The sail considered is square in shape (though the triangular sail features the shortest boom length) for designing a simpler attitude control actuator (Section 6). In the current configuration, the boom subsystem mass amounts to 0.142 of the sailcraft mass.

In applying Eq. (3.2.6) to the sailcraft design, the efficiency function $\eta\left(\theta_{\odot}, \mathcal{P}_{sail}\right)$ has to be computed via some model including the sail's surface scattering; $\theta_{\odot}$ and $\mathcal{P}_{sail}$ denote the angle of sunlight incidence on sail and the set of parameters characterizing the sail's surface, respectively. In the current case, we have used the vector scattering theory by Rayleigh-Rice (or RR-VST, for short) applied to SPS [12]. Considering the sail surface as isotropic, and characterized by root mean square roughness of 20 $nm$ and auto-correlation length of 100 $nm$ as the baseline sail in this mission concept, we have linearised about the normal incidence.

$$\begin{gathered}\eta\left(\theta_{\odot}\left[20 \;\; nm, 100 \;\; nm\right]\right) = 0.9534737 - 2.872\,10^{-4}\theta_{\odot}^{2} \\ 0 \leq \theta_{\odot} \leq 5^{o}\end{gathered} \tag{3.2.9}$$

where the sunlight incidence angle $\theta_{\odot}$ is expressed in degrees; thus, the thrust efficiency can be considered practically constant in this par-axial regime. Eqs. (3.2.5) and (3.2.9) are then inserted into Eq. (3.2.6) for computing the current sailcraft sail loading $\sigma$.

**Table 3.2.1:** Example of sailcraft that satisfies the concept of early-warning sail well below in radial distance than the Sun-Earth system L1

| **Input Values** | | |
|---|---|---|
| Gross P/L | 7 | $kg$ |
| CP1 Membrane | 2 | $\mu m$ |
| Reflecting layer (Al) | 90 | $nm$ |
| Boom linear density | 20 | $g/m$ |
| Chords net density | 0.5 | $g/m$ |
| Chords net frequency | 0.5 | $m^{-1}$ |
| Deployment mass ratio | 0.25 | |
| Sail shape | Square | |
| Fast-stream warning time | 140 | $min$ |
| Diagonal boom factor | $2\sqrt{2}$ | |
| **Output Values** | | |
| Sail area | 1196 | $m^2$ |
| Sailcraft sail loading, $\sigma$ | 11.51 | $g/m^2$ |
| Thrust efficiency, $\theta_\odot = 0$ | 0.95347 | |
| Lightness number, $\mathcal{L}_r$ | 0.1268 | |
| Length of one boom | 24.46 | $m$ |
| Sail side | 34.59 | $m$ |
| Mass of the booms | 1.957 | $kg$ |
| Sail mass | 4.809 | $kg$ |
| S/C – EMB sunward distance | 6.720 | $Mkm$ |
| Sailcraft mass | 13.77 | $kg$ |

### 3.2.3 Nominal orbital synchronization

An upgrade of the code used for the work described in Ref. [17] has been used here for propagating and optimizing the sailcraft trajectory with constraints in such a way that, year by year, the actual sailcraft motion looks like that of the ideal EMB-sync vehicle. We split this section in two subsections.

Synchrony loss

In the current problem of SEMB-sync, by spontaneous motion we mean that the sailcraft lightness vector has only the radial component different from zero: $\mathbf{L} = (\mathcal{L}_r, 0, 0)$ with the radial number taking on the design lightness number. This is a driven motion, of course, because the spacecraft gravitational motion is altered by the solar radiation pressure in a specified way. However, because $\mathcal{L}_r$ = constant and $\mathcal{L}_t = 0$ identically, no energy change is possible in this configuration, which we call the spontaneous motion, for short. Therefore, according to what said in Sec. 3.2.2 and from Eq. (2.2.28), the considered sailcraft's spontaneous motion is described in HIF by

$$\begin{aligned}
&\frac{d^2}{dt^2}\mathbf{R} + \frac{\mu_\odot}{R^3}\mathbf{R} = \frac{\mu_\odot}{R^2}\mathbf{L}_r\mathbf{r} + \sum_{k=1}^{N_{ncb}} \mathbf{P}_k \\
&t \equiv TDB \\
&epoch = 2022 - 07 - 05 \ \ 00:00:00 \ \ \text{UTC} \\
&\mathbf{R}_0^{(sph)} = \begin{pmatrix} 0.0449204 \ \ \text{AU} \\ 180^o \\ 0^o \end{pmatrix}, \mathbf{V}_0^{(sph)} = \begin{pmatrix} 1.294961 \ \ km/s \\ 90^o \\ 0^o \end{pmatrix} \\
&\mathcal{L}_r = 0.12688, \ \ N_{ncb} = 3 \ \ (\text{Earth-Moon, Jupiter } \textit{and} \text{ Venus})
\end{aligned} \tag{3.2.10}$$

In Eq. (3.2.10), the initial position and velocity of the sailcraft are assigned in spherical coordinates relative to the heliocentric orbital frame of EMB defined as: the x-axis is parallel to **r**, while the z-axis coincides with the direction of the orbital angular momentum of EMB. The y-axis completes the positive triad. We denote this frame of reference by EMB-HOF.

The planets perturbing the sailcraft in this mission concept are (1) the Earth-Moon system (considered here as a whole), (2) Jupiter, and (3) Venus. The disturbances from the other planets are negligible in the current context. Since the smallest synchronization time period is 1 year, let us see what happens if we propagate the sailcraft described in Tab. 3.2.1 by Eq. (3.2.10) for 1 year. We visualize the results in EMB-HOF; par-

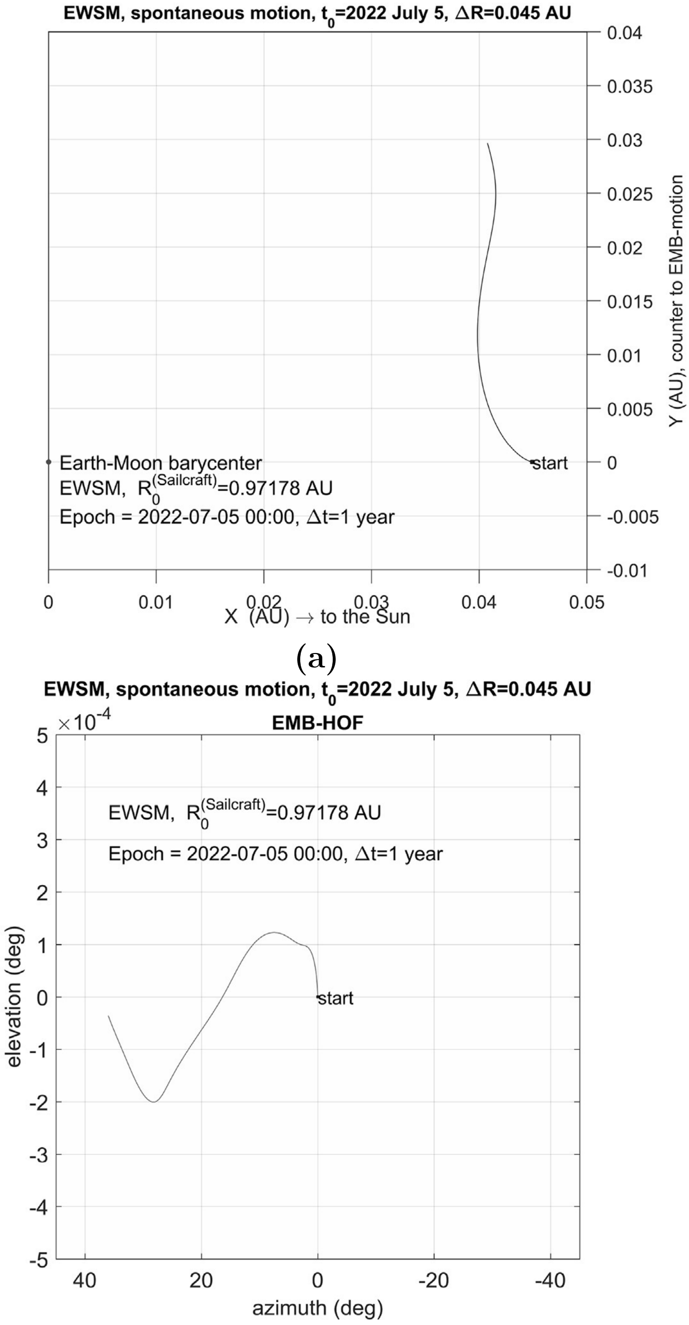

(a)

(b)

**Figure 3.2.3:** (a) sailcraft drifting, under the gravitational disturbances of the Earth-Moon system (mainly), Jupiter, and Venus, as it would appear in EMB-HOF. At epoch, the vehicle is synchronous with the Earth-Moon barycentre. (b) sailcraft's angular evolution as observed in EMB-HOF.

ticularly important are (I) the sailcraft relative trajectory, and (II) the angular motion in the celestial sphere centred on EMB. Fig. 3.2.3 shows path-I (left) and path-II (right) of the spontaneous motion of the sailcraft. The drift, due to the gravitational perturbations of Earth-Moon, Jupiter, and Venus, brings about a strong loss in synchrony whereupon the vehicle may be used only for very limited time. This tells us that the radial component of the lightness vector **L** is necessary, but not sufficient for achieving an efficient long-lasting SEMB-sync mission; in other words, we must use the transversal components of **L** for trying to balance the gravitational perturbations. In next subsection, we will deal with one of the potential solutions, a simple one (at least in principle).

### Controlled orbit

In this thesis, the strategy to drift balancing is called the baseline synchrony profile (BSP). The BSP concept entails the achievement of synchronization on average (SA) - during each year of the sailcraft orbit - by resorting to the normal number and the transversal lightness number in Eqs. (2.2.29) and (2.2.32). In the current problem, if we carry on with $\mathcal{L}_n$ negligible, then by acting through $\mathcal{L}_t \neq 0$ (even if $\mathcal{L}_t \ll \mathcal{L}_r$) we could change energy and angular momentum direction a bit, but sufficiently to balance drift. Thus, we expect to get a sailcraft batch-synchronized, even though the planetary disturbances accumulate over time Sec. 3.2.3.

The synchronization on average is not a trivial concept. We deem it depending on the observed angular spreads of CMEs and the distribution of the inside particles [61]. Since this task appears complicated indeed (by lacking data about the internal particle distribution), we have chosen to begin with a simple form of it. We try to achieve a good annual synchrony by considering four 3-month arcs per orbit: each arc is driven by sail attitude constant in HOF. This should simplify the attitude control realization, and reduce the sailcraft mass. For each of the subsequent years, the 4-arc re-orientation manoeuvre strategy will have to be repeated.

Let us consider the year from July 5, 2022 to July 5, 2023, and divide the sailcraft orbit into four arcs. In a generic segment, say, $j \quad (j = 1, \ldots, 4)$ of duration $\Delta t_j$, we use the following piece-wise constant **L**

$$\begin{aligned} &\mathbf{L}^{(j)} = (\mathcal{L}_r \ \mathcal{L}_t \ \mathcal{L}_h)^{(j)}, \quad \left|\mathcal{L}_h^{(j)}\right| \ll \left|\mathcal{L}_t^{(j)}\right|, \ \langle \mathcal{L}_n^{(j)} \rangle \\ &\sum_{j=1}^{4} \Delta t_j = 365.25 \ \text{days} \end{aligned} \tag{3.2.11}$$

In words, if one manages to keep the normal number noise very small, one can replace it by its null average; we assume this may be a workable scheme (to be verified *a-posteriori*). Here, we like to know whether the use of the transversal component of **L** may bring off the SA condition.

**Remark-2**. Vector Eq. (2.2.28) tells us that, similarly to rocket propulsion, one could ignore the structure of the propulsion system (i.e. the sail system here), and solve the astrodynamical problem(s) of interest by focusing only on the control (i.e. **L** here) and, for optimality with respect to some index of performance, on the control partial derivatives. In the case for solar sailing, given the mission class, the sailcraft's specific area (i.e. the reciprocal of the sail loading) is proportional to the max value of $|\mathbf{L}|$ for carrying out the mission [[12], Sect. 8.3]. This is what we did (in the current context) by first determining the value of $\mathcal{L}_r$ for SEMB-sync via Eqs. (3.2.1)–(3.2.5), and then proceeding to the sailcraft mass breakdown (Section 3).

Thus, in addition to the last of Eq. (3.2.11) as an equality constraint, the key point is to solve the following two-point boundary problem:

$$\begin{aligned}
&\frac{d^2}{dt^2}\mathbf{R} + \frac{\mu_\odot}{R^3}\mathbf{R} = \frac{\mu_\odot}{R^2}\left(\mathbf{L}_r\mathbf{r} + \mathbf{L}_t\mathbf{h}\times\mathbf{r}\right) + \sum_{k=1}^{N_{ncb}}\mathbf{P}_k \\
&t \equiv TDB \ , \ \ epoch = 2022-07-05 \ \ 00:00:00 \ \ \mathrm{UTC} \\
&\ N_{ncb} = 3 \ \ (\text{Earth-Moon, Jupiter } \textit{and} \text{ Venus}) \\
&\mathbf{R}_f^{(sph)} = \mathbf{R}_0^{(sph)} \ \ , \ \ \mathbf{V}_f^{(sph)} = \mathbf{V}_0^{(sph)} \\
&\sum_{j=1}^{4}\Delta t_j = t_f = 365.25 \ \ \text{days}, \Theta = \{\alpha_i\}\,, \ \ i = 1...4
\end{aligned} \tag{3.2.12}$$

where vectors $\mathbf{R}_0^{(sph)}$ and $\mathbf{R}_0^{(sph)}$ are given in Eq. (3.2.10), and $\alpha_i$ is the azimuth of the sail axis during the orbit's arc-$i$. Eq. (3.2.12) contains 7 equality constraints and 8 control parameters, namely, the durations and the sail-axis azimuthal angles of the four arcs; the sail-axis elevations have been set to zero according to what we said about the normal numbers in Eq. (3.2.11). Thus, this problem has one degree of freedom suggesting that the four-arc solution (if any) would be the simplest one in the 1-year synchrony. We will use such degree of freedom for obtaining a spread about the ideal synchronous orbit less than $\pm 5^o$ in azimuth as seen from the EMB. This should increase the signature of the storm alarm (raised by the sailcraft towards ground stations) via the wind's magnetic field. Equivalently, the sailcraft-EMB distance (expressed in AU) may straggle inside the circle of radius 0.004 centred on the nominal point (-0.045, 0) in the XY-plane of EMB-HOF. This problem has been dealt with by Non-

**Table 3.2.2:** Control parameters that synchronize the sailcraft orbit from 2022-07-05 to 2023-07-05 in the sense of Eq. (3.2.12). Arc-0 denotes the end-point of the transfer trajectory that moves the sailcraft from the injection point (on the Earth's outer sphere of influence) to the first nominal station point.

| Arc No. | Duration [day] | Azimuth [deg] | $L_r$ | $L_t$ |
|---|---|---|---|---|
| 0 | | 0 | 0.12688 | 0 |
| 1 | 88.80356 | −0.619 | 0.12686 | −0.0012613 |
| 2 | 93.38379 | 0.495 | 0.12687 | 0.0010087 |
| 3 | 89.71731 | −0.520 | 0.12687 | −0.0010596 |
| 4 | 93.34569 | 0.569 | 0.12686 | 0.0011594 |

Linear Programming (NLP). Two modified versions of the basic Levenberg-Marquardt method have been used. Though the guessed solution was found by using the same method in two logical steps, 96 iterations were necessary to converge; net processing time of 4.4 s came from a workstation based on a 12-core 64-bit CPU on which our Fortran 95/2003 based NLP code runs. The solution to the problem is shown in Tab. 3.2.2 and Fig. 3.2.4

This sequence of alternate decelerations and accelerations - in terms of photon sailing - allows the sailcraft to keep the drifting within the assigned tolerances. Every three months (approximately), the sail axis must be re-oriented by slightly more than 1 deg

One should note that each year of Sun surveillance has its own sequence of manoeuvres simply because (mainly) the planetary gravitational perturbations are not equal to those of the past years. Anyway, the challenge to get precise transversal lightness number values of about 0.001 appears now clear.

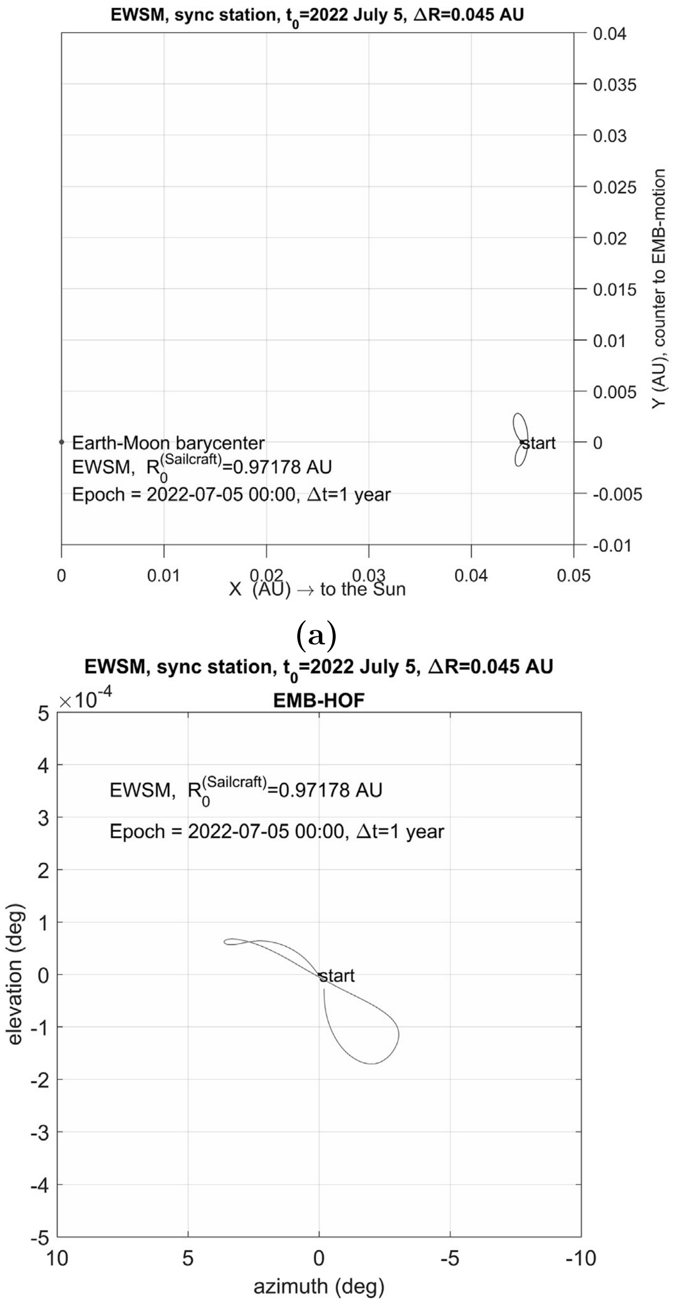

**(a)**

**(b)**

**Figure 3.2.4:** Evolution of the sailcraft described by Eq. (3.2.12) driven by the piece-wise control reported in Tab. 3.2.2. The curves on parts (a) and (b) should be compared with Fig. 3.2.3

## 3.3 Earth-to-Mercury and Earth-to-Mars

Every year new missions are proposed and designed to explore regions not completely known of our solar system. Instead the level of dynamical models accuracy and increasing of the low thrust ion engine readability, every year the available power for mission energy is higher. Some mission like Babi-Colombo wants to reach the closest planet to the Sun, Mercury. To achieve this purpose the mission analysts and trajectory designers found a trajectory that requires several swing-bys (9 in total) and around 7 years.

Using a Solar Photon Sailing that use the solar radiation pressure as propulsion system, to reach Mercury could be even simpler for several reasons:

- getting closer to the Sun the available energy it is higher;
- due the radiation pressure there are not required swing-bys
- there is not limit due to launch windows

The advantage to reach Mars is prevalently the third one in the list

In this section we are going to introduce the parametric work to make an orbital change from an Earth-like circular orbit to: 1) a circular planar orbit with the radius equal to the semi-major axis of Mercury orbit; 2) a circular planar orbit with the radius equal to the semi-major axis of Mars orbit . This preliminary analysis wants to empathise the importance of the physical model used to describe the sailcraft. A similar analysis is made in Ref. [62] using the perfect reflection model for the Mercury case. The Fig. 3.3.1 shows shortly the concept of this where the dashed lines are the planet's orbits and the continuous line are the hypothetical trajectory of the SPS.

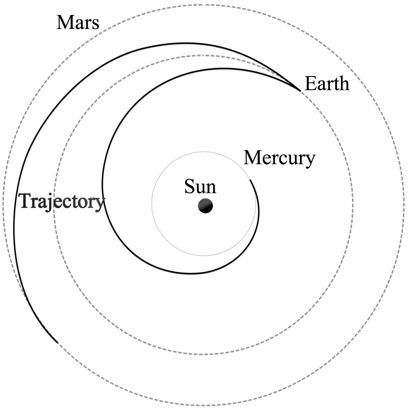

**Figure 3.3.1:** The concept of the mission under analysis, the dashed curves are the planet's orbit and the continuous lines are the sailcraft trajectories

We decide to use two different reflection model introduced in the Chap. 2 for a flat sail surface. The dynamics is a kelperian 2 body problem with only the solar radiation pressure.

### 3.3.1 Earth to Mercury

Firstly, we analyse the case for Mercury. Selecting the characteristic acceleration $a_c = 2\frac{TSI}{c\sigma}$ in a range $[0.2, 0.8]$ $mm/s^2$ for the specular reflection model, we reproduce the same result of Ref. [62]. To produce these trajectories we divide the integration time into 10 arcs with constant attitude in the HOF reference frame, where HOF is define in the Sec. 2.2.3. We are going to present three trajectories for representative cases of characteristic acceleration. In Fig. 3.3.2 we collect the trajectories for the specular and optical reflection model using a $0.3 mm/s^2$ for characteristic acceleration. The time of travel for the specular case is about 2.214 years, but the optical model requires 0.1043 years more, it is equivalent to 38 days.

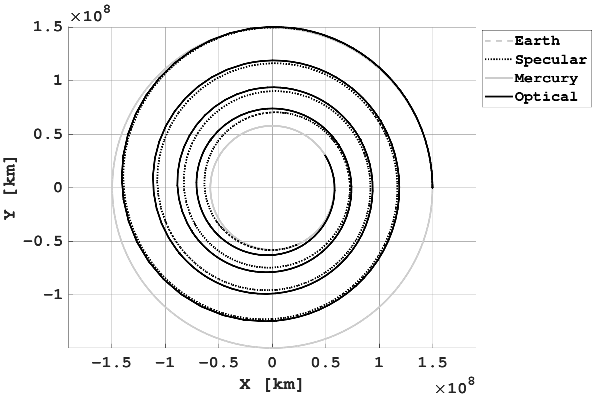

**Figure 3.3.2:** Mercury's trajectory comparison for $a_c = 0.3 mm/s^2$

An intermediate case is selected with an $a_c = 0.5 mm/s^2$. For this case, the time of travel for the specular reflection model is about 1.3698 years and there is again a difference of about 38 days that divides the two solutions (1.4743 years). Differently from before, as it is shown in Fig. 3.3.3, the sailcraft needs about $2-2.5$ revolutions about the Sun to reach the target orbit. The divergence between the trajectories is evident only in the last part, this is attributable to the integration time shorter than before.

Finally, the $a_c = 0.7 mm/s^2$ is selected to empathize the divergence of the time of travel between the two models decrease and it is equal to about 21 days. In the specific the trajectories in Fig. 3.3.4 the specular reflection

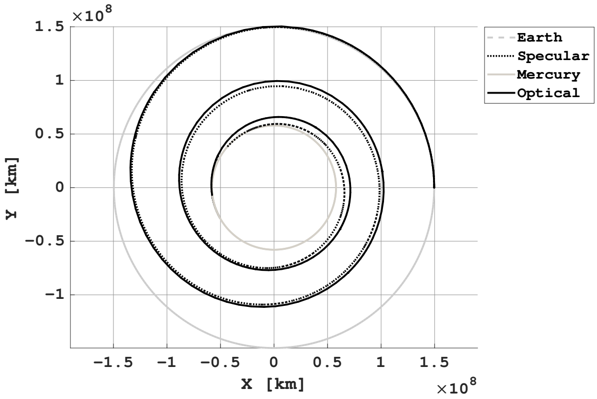

**Figure 3.3.3:** Mercury's trajectory comparison for $a_c = 0.5 mm/s^2$

model is about 1.3698 years and there is again a difference of about 38 days that divides the two solutions (1.4743 years).

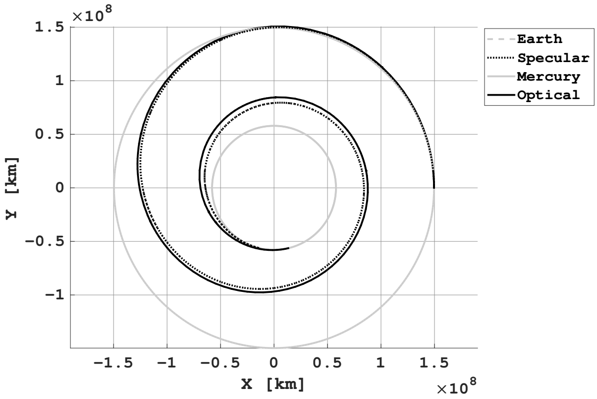

**Figure 3.3.4:** Mercury's trajectory comparison for $a_c = 0.7 mm/s^2$

To better identify the deviation between the two models we show the time of flight over the characteristic acceleration $a_c$ and $\sigma$. In Figs. 3.3.5 and 3.3.6 are plotted in dotted style the results for the specular reflection model, the same result was obtained in Ref. [62]. The continuous curve in both figures represents the solution using the Fresnel Optical reflection model, these have a similar behaviour with a sort of translation along the abscissa's axis. The sail loading $\sigma$ is in the range $[45.4, 11.35]$ $g/m^2$.

From a minimum time of 1 year with a very futuristic value of characteristic acceleration equivalent to $11.35 g/m^2$ for the sail loading to a time of flight around 3.5 years for a $\sigma = 45.4 g/m^2$, this value will be achievable in the close future.

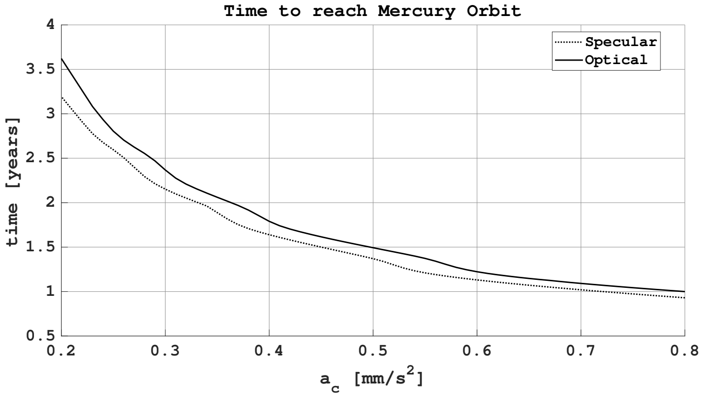

**Figure 3.3.5:** Time of flight for Specular and Optical model in function of characteristic acceleration $a_c$

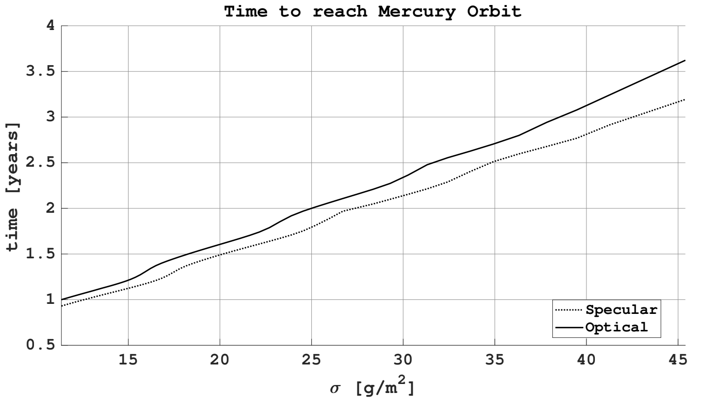

**Figure 3.3.6:** Time of flight for Specular and Optical model in function of sail loading $\sigma$

### 3.3.2 Earth to Mars

The case to Mars wants to show the difference of time travel respect the low thrust and the impulsive case. With the same range of characteristic acceleration we obtain the minimum time of travel for the orbital change.

With a characteristic acceleration equal to $0.3mm/s^2$, the first case with the specular reflection model takes 2.6861 years to reach Mars, as expected the other model needs more time to achieve the objective target, in the specific 36 days more for a total of 2.7853 years. Fig. 3.3.7 shows that are needed closely 2 revolution about the Sun to reach the final orbit.

As made before for Mercury, an intermediate case with $a_c = 0.5mm/s^2$ is selected to report the time of flight with both reflection model. The are separated by about 60 days an in the specific the specular (dotted curve in Fig. 3.3.8) and the Fresnel model (solid curve in Fig. 3.3.8) take 1.5362 and 1.7024 years, respectively. A little more than a revolution about the

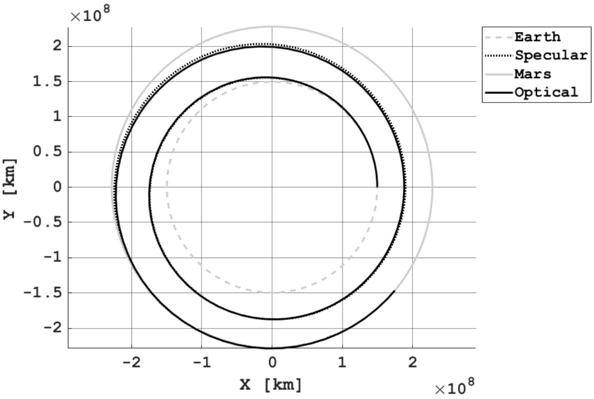

**Figure 3.3.7:** Mars's trajectory comparison for $a_c = 0.3mm/s^2$

Sun is required to achieve the selected target.

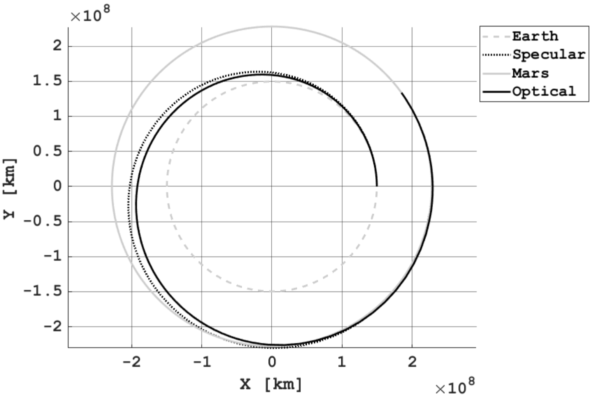

**Figure 3.3.8:** Mars's trajectory comparison for $a_c = 0.5mm/s^2$

The $a_c = 0.7mm/s^2$ is studied to empathize the divergence of the time of flight between the two models decrease for this case too, for the Mars case is equal to about 19 days. In the specific the trajectories in Fig. 3.3.9 required 1.2855 years for the specular reflection model and 1.3401 years for the Fresnel's one.

The entire set of characteristic accelerations are studied and the results are collected in Figs. 3.3.10 and 3.3.11 where the divergence reduction increasing the $a_c$ is equivalent to the divergence reduction decreasing the $\sigma$. The gap in time of flight between the two models is attributable to the non linearity of the problem. Same result was obtained in literature.

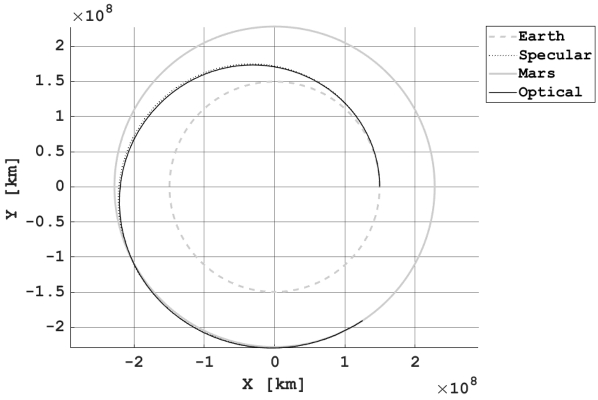

**Figure 3.3.9:** Mars's trajectory comparison for $a_c = 0.7 mm/s^2$

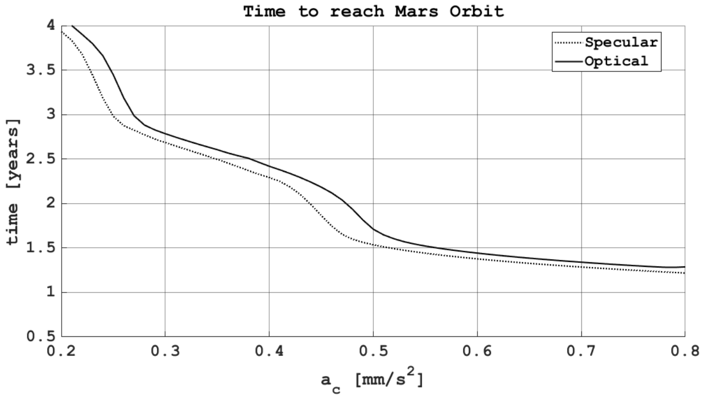

**Figure 3.3.10:** Time of flight to Mars for Specular and Optical model in function of characteristic acceleration $a_c$

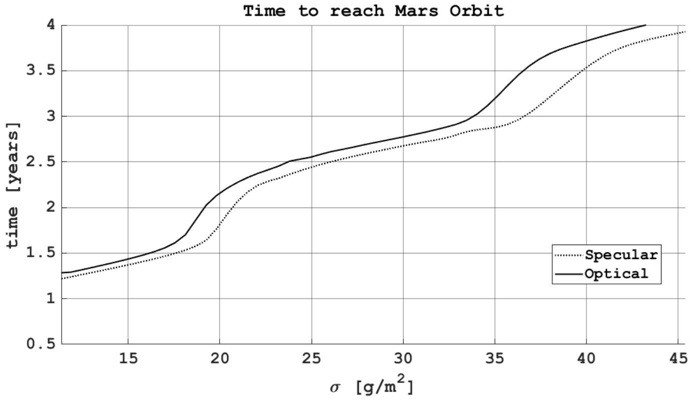

**Figure 3.3.11:** Time of flight to Mars for Specular and Optical model in function of sail loading $\sigma$

## 3.4 Considerations

The entire comparison between these reflection model empathize the importance of a accurate model for the mission design. A different reflection model could introduce an important deviation from the optimal trajectory obtained with another one. This analysis empathizes that exists a divergence in the time of flight between the two reflection models reducing the performance of the sailcraft. A no-linear behaviour is present in both mission, this is evident in the central of Figs. 3.3.5, 3.3.6, 3.3.10, 3.3.11

For a certain range of characteristic acceleration the difference between both reflection model increase significantly to decrease again. In the considered range of $a_c = [0.2, 0.8]$ $mm/s^2$, for the Mercury case we identify three of this region but these are more evident for the Mars case where there are two of these. This behaviour could be imputable to the theory that exist an optimum value of $\sigma$ for each mission [12]. A better performance of $\sigma$ does not mean a better result.

# 4

# High Fidelity Thrust Model

In space mission analysis a small deviation on used dynamical model could produce a large trajectory deviation from the optimal solution. As an example, for decades the total solar irradiance (TSI) was considered a solar constant. On the other hand, only satellites' measures proved that it did not. Lots of studies about solar photon sailing's (SPS) trajectory considered the solar radiation pressure a constant assigned by the analyst, but in some recent works it was emphasized how the TSI's fluctuation produced a significant deviation from the nominal trajectory, involving missing the rendez-vous with the planet [18, 63].

The IKAROS mission (JAXA, May 2010) and NanoSail-D2 (NASA, September 2010) have demostrated the reality of SPS and, with three further mission projects in progress in USA and Japan, the study of more accurate thrust model is a main aim of the scientific community. Starting from the well known specular reflection model and the optical proposed by [11]. The knowledge of the problem gradually increase to complexity [17, 51] to reach today a reflection model that consider the vectorial scattering and the mean square roughness of the surface [52, 64]. Considering the sail as a flat surface begins to be a strong approximation. Therefore, in the last few years some publication starts to analyse the sail surface phenomena and its consequences with the thrust vector and the center of pressure with a study using a finite element method (FEM) approach [65–68].

The activities here proposed wants to consider a real sample of solar sail. Taking as an example the work proposed by [69], it is studied the effects of a realistic joint that it produces on the deformations of a solar sail membrane. We investigate also how an ageing could be reflected on the sailcraft performances.

## 4.1 Instrument setup

As point out from the previous sections, to design a realistic interplanetary trajectory is fundamental to use an accurate thrust model. With solar propulsion system this is even more important because we could not turn off the thrust source, the Sun. Therefore, it is important to analyse in details how the photons interact with the surface, but at the same time how a membrane deformation modify its shape and its incidence with respect to the sunlight. The aim of this chapter is focused on this second aspect. To analyse the surface deformation we decide to proceed with an experimental measure on a solar sail membrane samples exposed on several work conditions.

We decide to use a laser sensor that measure the distance between itself and the target. It is placed on a carriage, part of a bigger hardware built for this purpose. The sensor is moved over the surface by a robot composed of a structure fixed to the ground and two carriages. The carriages take advantage of the cavity of aluminium profiles 30x30 mm with four hollows chosen as structural elements. Considering the strain and the masses these profiles guarantee that the deformations and the bends of the structure are negligible for the purpose.

The two degree of freedom permit to identify the axis $x$ and $y$ of the instrument, thus the sensor's acquired data are a point-cloud in space. Fig. 4.1.1 shows the instrument in the project and design phase made with Autocad Inventor software. The digital prototyping permits the error correction during the design saving a lot of time in the construction phase.

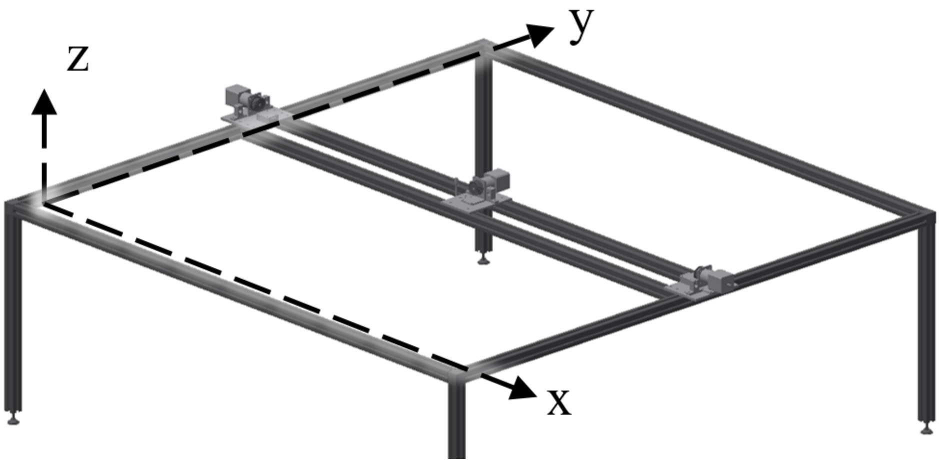

**Figure 4.1.1:** Reference frame of the equipment

The carriages are moved by stepper motor NEMA17 with gearbox 1:51 that permit to achieve a 2 $\mu$m precision on positioning in the work-space using fixed toothed belts.

Motors control is delegated to electronic shields Phidgets® (*Phidget-Stepper Bipolar HC*) connect to the computer by USB cables. They are linked to MATLAB® through a **C#** library written for this purpose.

The chosen laser sensor is produced by KEYENCE with the identify designation *IL-065*. The sensor measures the vertical displacement in a range of 20 mm with a repeatability of 2 $\mu$m using a red laser with a 655 nm wavelength. The sensor is connected to an analog-to-digital converter operating with 16bit used to sample the signal, then it is wired to Arduino where a batch filter is applied and finally connected to the **C#** library mentioned before via a USB cable.

To apply the tension to the samples, an internal fixed frame is built with three moveable platform each one equipped with a load cell (Fig. 4.1.2). The Tension is applied with a platform's linear displacement and the sensors are used to measure the load, they are connected to a Phidgets® bridge board and linked to a **C#** application. We used a Dacron wire to connect the platform to the eyelet putted on the sample.

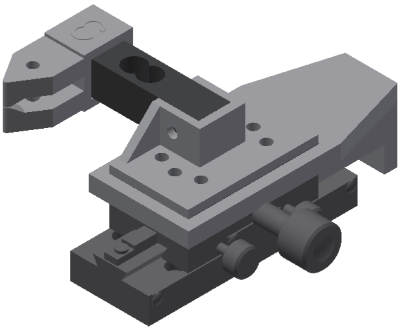

**Figure 4.1.2:** Moveable platform to apply tension to the samples

To conclude we show Fig. 4.1.3 where it is observable the complete instrument and a sample is placed in the instrument working region. The stepper motor at the center of the working area is located on the X axis carriage where the laser sensor is located too. The suspended structure permits to bring the cables to the electronic controller shields. On the left, one of the Y axis motor is clearly visible.

Over the structural elements on left and right are visible the white tooth belts. At right, under the table we could identify the electronic shields immediately over the personal computer.

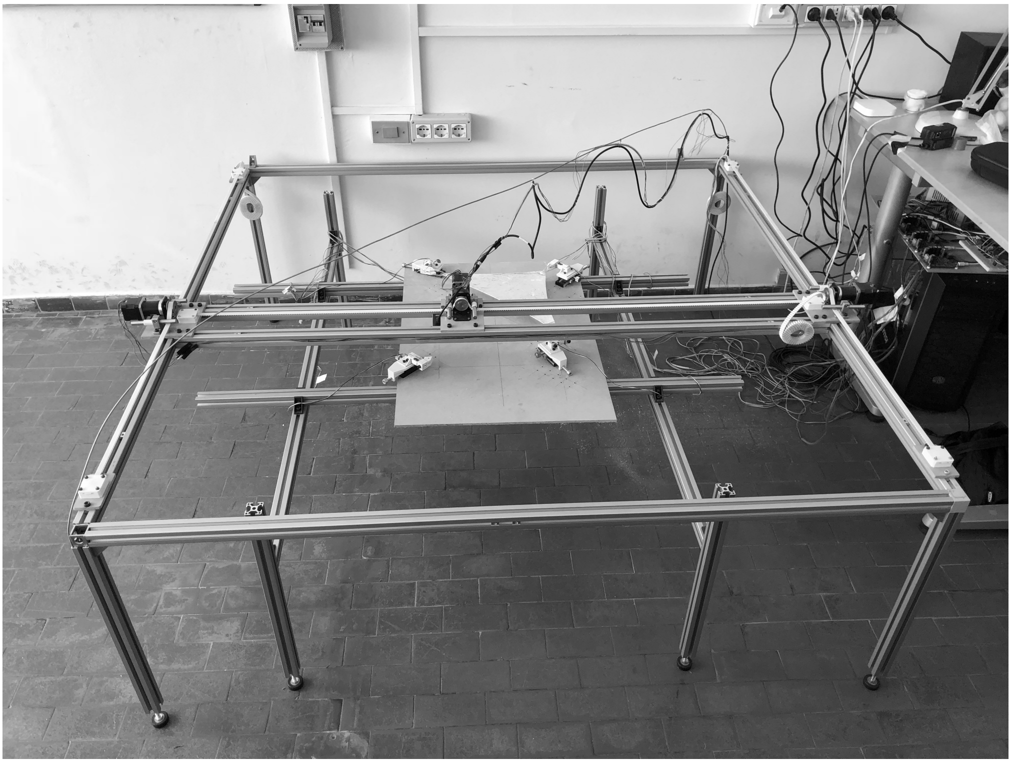

**Figure 4.1.3:** Photo of the equipment

Into the working are of the instrument it is possible to identify four linear displacement platform, in this current work we are going to use only three of these, but everything is designed to host square sail samples.

The following section we are going to describe the samples and how they are processes

## 4.2 Samples preparation

The solar sail material selected is a CP1 polyimides film delevoped by NASA and produced under license to *SRS Techologies* through Nexolve Company. The samples are a membrane of CP1 with 2.5 $\mu$m of thickness and a coating of 100 nm of Vacuum Deposited Aluminium. Their shape is a right-angled triangle with a 30 cm length cathetus.

The samples arrived from the industry on a plastic support used for the fabrication and the transportation.

To emulate with the highest fidelity a solar sail we decide to apply a support to the vertexes with a layer of Kapton with thickness of 25.4 $\mu$m, the thinnest film available. In the areas' barycenter we insert an eyelet to permit the passage of a Dacron wire. In the Fig. 4.2.2 is possible to observe a detail of one sample where the opaque surface is the Kapton support and the white ring is the 3D printed eyelet. Into Fig. 4.2.1a we observe the sample with a ultra smooth surface on the transfer plastic support where we applied the Kapton reinforcement previously described. Into Fig. 4.2.1b we show the same sample cleaned by the exceeding Kapton material before applying the support on the other sample face.

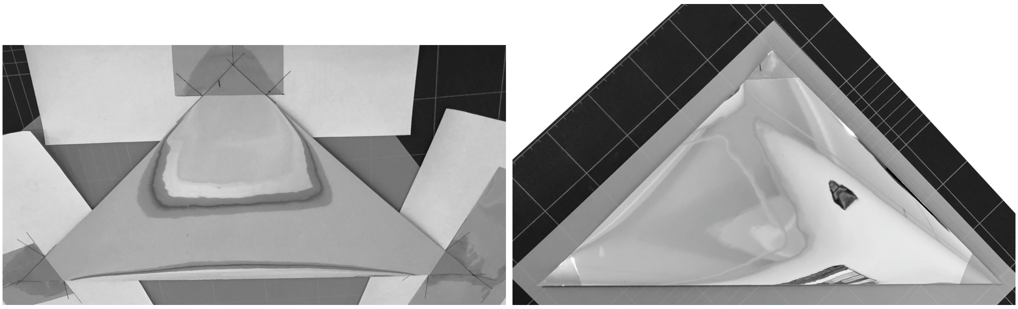

**(a)** Application to a generic sample of Kapton support

**(b)** Generic sample after removing the Kapton excess

**Figure 4.2.1:** Generic sample during application of Kapton support

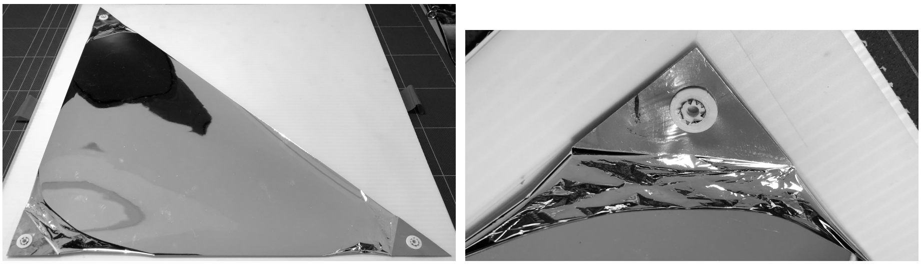

**(a)** Generic sample with applied the eyelets

**(b)** Detail to no stress eyelet

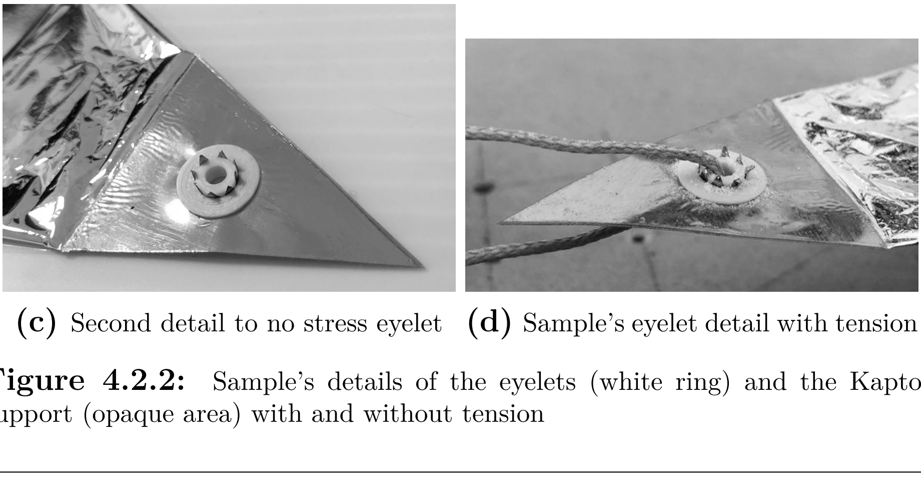

**(c)** Second detail to no stress eyelet

**(d)** Sample's eyelet detail with tension

**Figure 4.2.2:** Sample's details of the eyelets (white ring) and the Kapton support (opaque area) with and without tension

In conclusion Fig. 4.2.2 show firstly the entire sample and then details of eyelets already described for different vertex. Into Fig. 4.2.3a we show the sample removed from the plastic support and put in tension. The sample results smooth without creases with the only presence of the wrinkle behaviour. To simulate a plausible degradation of the surface due to the packaging, this is processed with a sort of packaging (Figs. 4.2.3b–4.2.3e). Once unpacked and reset on the tensional set up, it presents both the effects desired - wrinkles and creases - as we could see in Fig. 4.2.3f. In the next section we are going to introduce the working condition for the testes and the acquisition campaign.

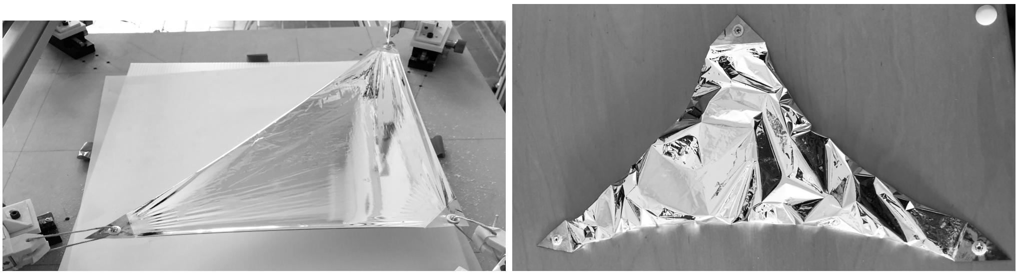

**(a)** Generic sample on strain immediately after removed from delivery support

**(b)** Generic sample without stress

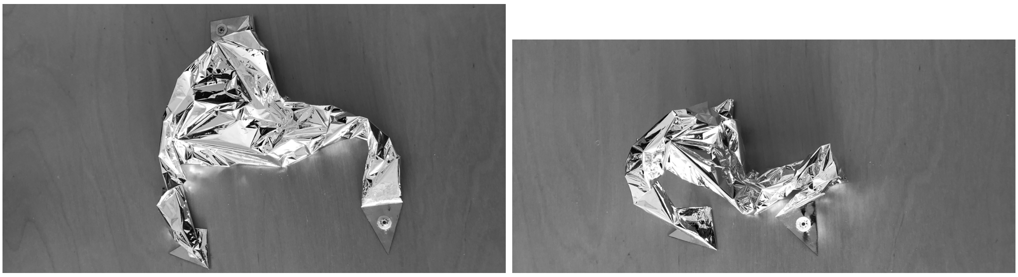

**(c)** Generic sample after the first step packaging

**(d)** Generic sample after the second step packaging

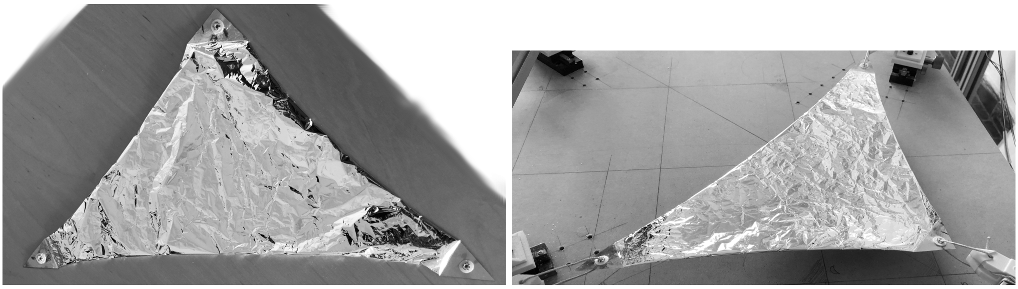

**(e)** Generic sample without stress after packaging

**(f)** Generic sample on strain immediately after packaging

**Figure 4.2.3:** Packaging degradation process

## 4.3 Experimental Acquisition Campaign

To proceed with the experimental acquisition campaign we have to identify those condition could represent the reality. To select the tension loads to apply we visually decide the first acceptable tension.

Firstly, we have to calibrate the load cells. To do that we decide to consider the no tension case when a generic sample is correctly placed into the inner frame and it starts to unroll the edges. Fig. 4.3.1 is considered the discussed case and the identifier letter for each platform are shown too.

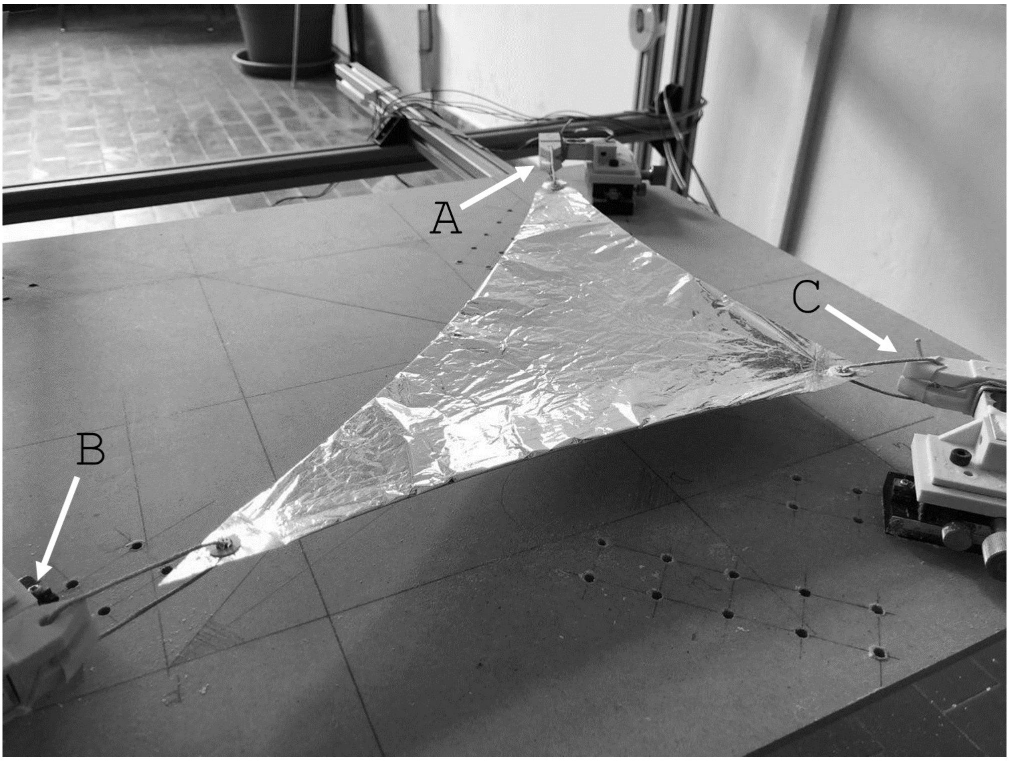

**Figure 4.3.1:** Starting load, with the identifier of tensional platforms

Identified the initial point, we start to increase the applied tension manually moving the linear displacement platform C. Every millimetre in displacement is considered as a case of study with a scanning procedure. We identify substantially three representative cases that show the predicted behaviour. The intermediate cases are simply transition between the representative cases.

Into the first case, the samples reduce the initial curvature and they start deploying the area at the edges. The location of the applied tension

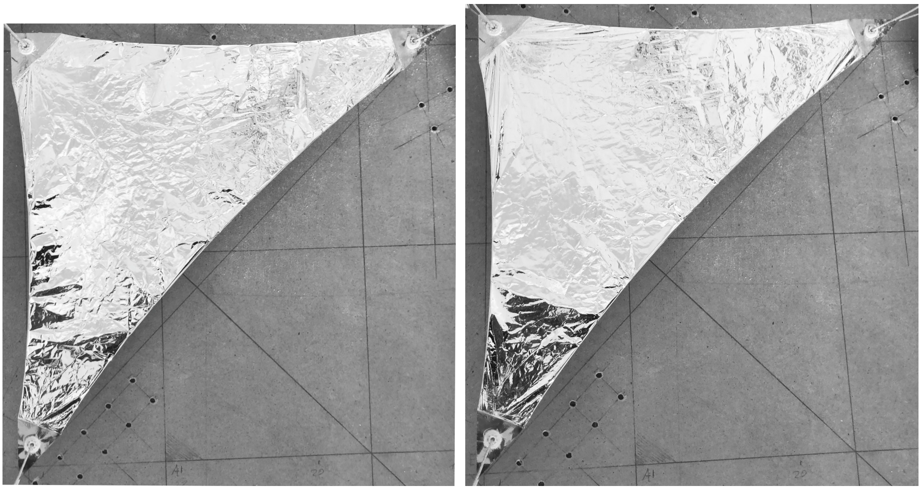

**(a)** Top view of the first load of Tab. 4.3.1

**(b)** Top view of the second load of Tab. 4.3.1

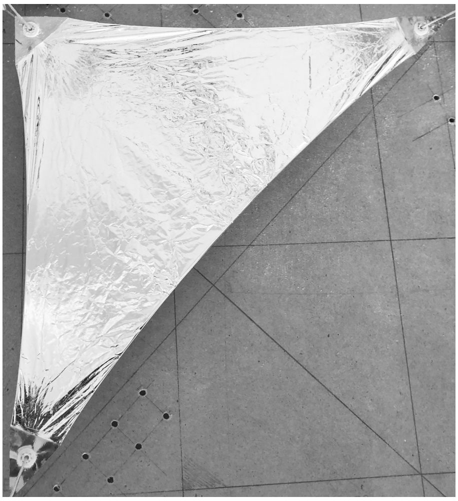

**(c)** Top view of the third load of Tab. 4.3.1

is indicated with the letters and the correspondent vertex is shown in Fig. 4.3.2a

Subsequently, into the second case, some wrinkles start to show up, it is shown in Fig. 4.3.2b where it is evident the presence of wrinkles strictly in the regions close to the Kapton support and the creases randomly visible all around the surface.

Lastly, the wrinkles are relevant starting from a vertex arriving to the other two trough the entire membrane (Fig. 4.3.2c).

The values summarizes in the Tab. 4.3.1 are the tensions for the selected representative cases of study discussed above. All measures could be considered with an error of $\pm 10^{-3}$ N due by the repeatability of the load cells. We replicate the acquisition process for all three available samples.

**Table 4.3.1:** Summarize of all tension's cases for each vertexes

| Case | A [N] | B [N] | C [N] |
|---|---|---|---|
| First | 0.10 | 0.10 | 0.05 |
| Second | 0.20 | 0.21 | 0.10 |
| Third | 0.31 | 0.30 | 0.16 |

## 4.4 Experimental Analysis

Acquired the points cloud we could rebuild the shape sample that its mesh is composed by a population of triangles, named *elementary cell* approximately of $0.5mm^2$, where we define a normal for each one. We analyse the probability histogram for the azimuthal ($Az$) and zenithal ($\alpha$) angles for every normal to identify a probability density function (PDF) to describe the phenomena.

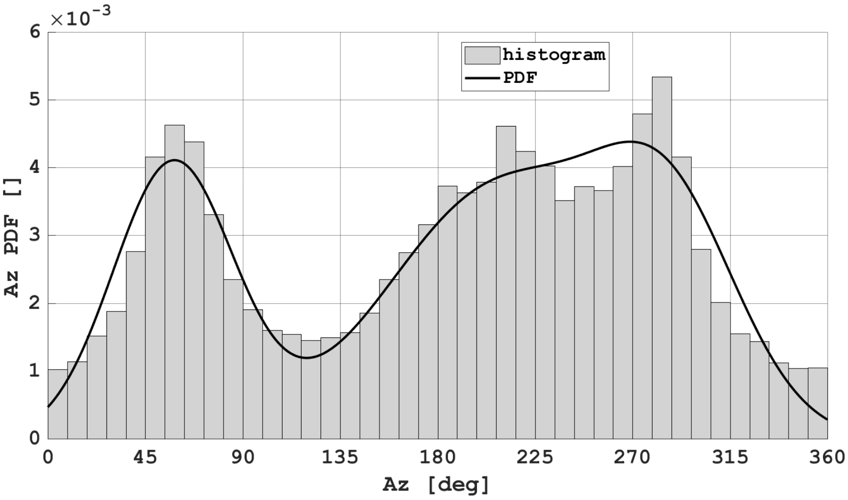

**Figure 4.4.1:** PDF azimuthal

The Figs. 4.4.1 and 4.4.2 are the results for the third sample with the second load. It is clear that a PDF could describe the phenomena. Comparing the results for the third sample with the other two it is possible to identify a sort of scheme in the results that gives a validation between the experimental data. The Fig. 4.4.3 shows the PDFs for the three studied samples and they are qualitatively comparable.

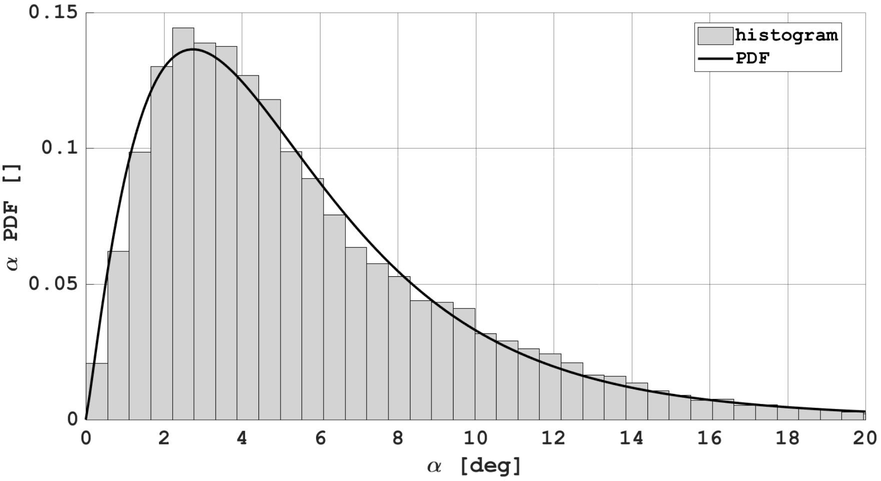

**Figure 4.4.2:** PDF zenithal

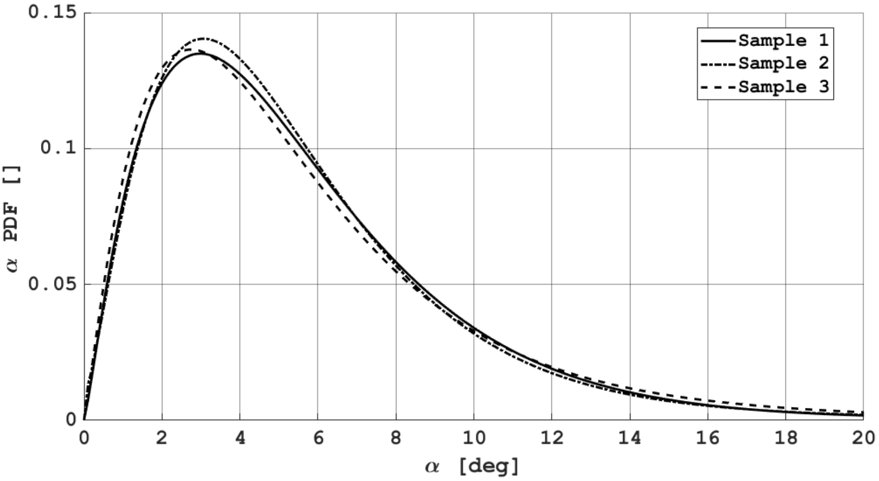

**Figure 4.4.3:** Comparation of PDFs' zenithal for all three samples

The sail surface deformation produce two different effect that affect the sailcraft performance.

The first one regards the reduction of the effective surface useful for thrust. Considering the mass expression and the its variations:

$$\begin{aligned} &m = m_{\mathrm{L}} + m_{\mathrm{S}} = m_{\mathrm{L}} + \rho d \mathcal{A} \\ &\delta m = \rho d \delta \mathcal{A} + \rho \mathcal{A} \delta d = 0 \\ &\frac{\delta d}{d} = -\frac{\delta \mathcal{A}}{\mathcal{A}} \end{aligned} \tag{4.4.1}$$

then a variation of the area means a variation of thickness. Considering the sail loading expression

$$\begin{aligned}\sigma_0 &= \frac{m}{\mathcal{A}} \\ \sigma_w &= \frac{m_\mathrm{L} + m_\mathrm{S}}{\mathcal{A} + \delta\mathcal{A}} \\ &= \frac{\sigma_0}{(1 + \delta\mathcal{A}/\mathcal{A})}\end{aligned} \tag{4.4.2}$$

Again, a variation of the effective area means a variation of the project $\sigma_0$.

The second effect regards the normal direction's deviation. Indeed, as it is shown in Figs. 4.4.1 and 4.4.2 the normal's azimuthal and zenithal angles are not zero.

We could now investigate how these variations affect the lightness vector calculation reformulating the Eq. (2.1.4) adding both effects: area's variation ($\delta\mathcal{A}$); normal direction's deviation ($\delta\mathbf{n}$).

$$\mathbf{L}_w = f\left(\mathcal{A} + \delta\mathcal{A}, \mathbf{n} + \delta\mathbf{n}, \dots\right) \tag{4.4.3}$$

By the knowledge of the phenomena, it is clear that these variation are stochastic. This means that for an analysis in the following section a random values for azimuth and elevation angles are required to correctly design the X shape sailcraft. For each petal we randomly extracted form the PDFs the values using the subroutine RandomVariate of Mathematica 11.2. We would like to empathize that the area for the second load of third sample is reduced from the starting value with a reduction of about 12.60%. This decrease of effective are is due to two contributes: the mainly change of shape decreases the area of 10.78%; the wrinkles and creases produce 1.82% in area's reduction.

## 4.5 Deterministic comparation

Considering the Earth-Mercury transfer analysed in Sec. 3.3.1, we select three of the these optimal solutions with the Fresnel model ($a_c = [0.3, 0.5, 0.7]\ mm/s^2$). With these thrust profile we apply the obtained deviations. Firstly, we have applied area's deviation that produce an important deviation from the optimal final state. The position has a deviation radius between 14 and 18 million kilometres. The second main column shows the results where we have applied only the normal direction's deviation that produce a small error respect the previous case because the effective area does not change, only the direction. It is enough to roughly miss the objective of the mission. Lastly, the effects of both deviation is taken in account with very high deviation radius. In the Tab. 4.5.1 are summarized the errors on the final state for these different cases.

**Table 4.5.1:** Effects of Area's deviation ($\delta A$) and/or normal's deviation ($\delta\mathbf{n}$) on Fresnel optimal trajectory for three different values of characteristic acceleration $a_{c0}$

| $a_{c0}$ | $\delta\mathcal{A}$ | | $\delta\mathbf{n}$ | | $[\delta\mathcal{A}, \delta\mathbf{n}]$ | |
|---|---|---|---|---|---|---|
| | $\Delta X$ | $\Delta V$ | $\Delta X$ | $\Delta V$ | $\Delta X$ | $\Delta V$ |
| $\left[mm/s^2\right]$ | $10^6$ $[km]$ | $[km/s]$ | $10^6$ $[km]$ | $[km/s]$ | $10^6$ $[km]$ | $[km/s]$ |
| 0.3 | 18.85 | 6.97 | 0.174 | 0.044 | 19.70 | 7.35 |
| 0.5 | 14.75 | 4.91 | 0.455 | 0.279 | 14.78 | 4.99 |
| 0.7 | 16.89 | 6.09 | 0.155 | 0.199 | 17.35 | 6.31 |

The relevant error due by the variation of the area it is important to optimize again to identify a sort of $\Delta t$ to obtain the same objective. The Fig. 4.5.1 shows the two curves previously obtained and a new one adopting the deformed model described in previously section. The $\sigma_0$ on the abscissa is the ideal one (with a flat surface). This $\sigma_0$ does not consider the area variation but the model does. For an ideal $\sigma_0 = 30 g/m^2$ we obtain a $\Delta t = 133$ days more respect the optical model.

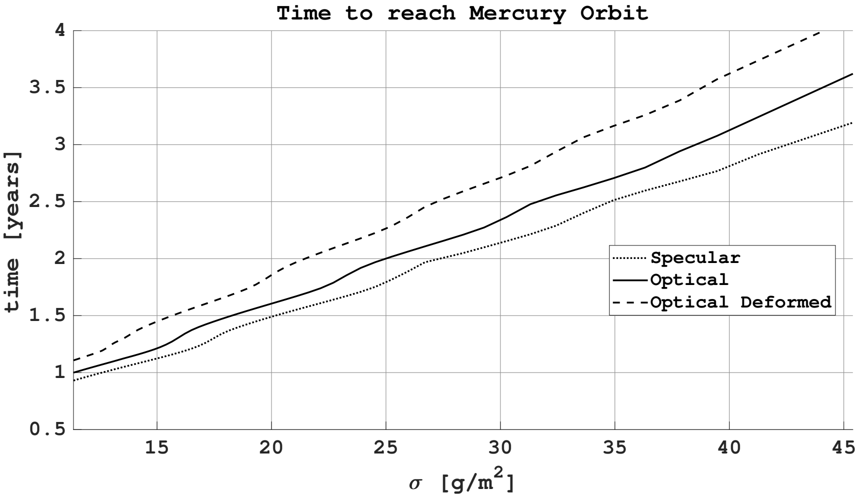

**Figure 4.5.1:** Time of flight for Specular, Optical and Optical Deformed model in function of ideal sail loading $\sigma_0$

If we consider in the sail design process and in the trajectory design the consequent area variation due by the ageing or the deployment of the sail, the abscissa becomes the real $\sigma_w$ and the time variation for the same value of sigma is $\Delta t = 1.09$ days (Fig. 4.5.2), due by the normal direction's variation only.

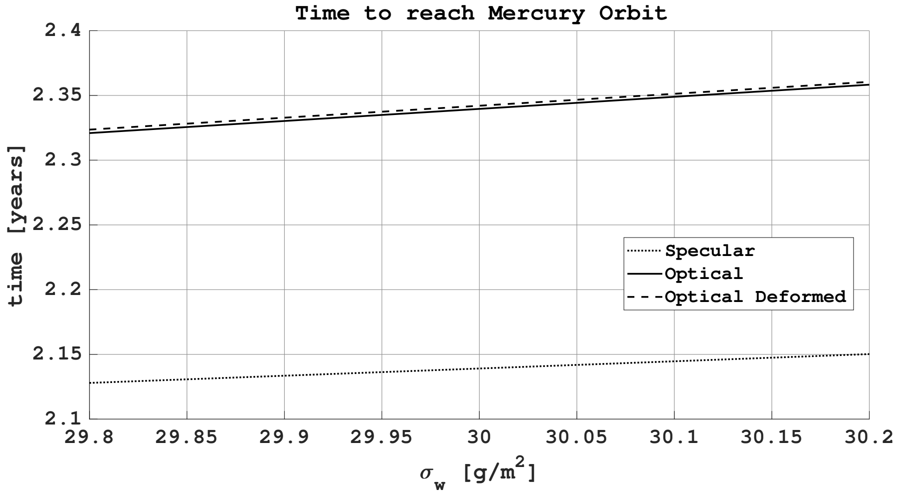

**Figure 4.5.2:** Time of flight for Specular, Optical and Optical Deformed model in function of real sail loading $\sigma_w$

# 5

# Conclusions

In conclusion this work has consider the importance to use for a mission design an accurate thrust model. Firstly, an overview of solar photon sailing thrust models has been presented starting from the specular reflection model through the optical one developed by Wright to the Fresnel one. To consider practically the difference between these reflection model several space mission has been studied.

An exploration mission of the binary star system of Alpha Centauri A/B has been carried out by using a stellar-photon sailcraft. The restricted three body problem has been studied in the general case of elliptical orbit of primaries with the sailcraft simultaneously irradiated by the light of the two stars. The mission has been divided into four parts: (a) the capture phase. This phase has been optimised by an angular momentum reversal strategy and needs about 16.8 years. A final circular orbit with radius of $\sqrt{1.5}$ AU has been selected in order to receive the same solar irradiance at 1 AU. (b) The polar orbit phase about Alpha Centauri A. The polar orbit is reached in 1.6 years, and in 3.3 years it returns equatorial. (c) The transfer trajectory from $\alpha$CenA to $\alpha$CenB. This phase is completed in 7.6 years and a final circular orbit about aCenB is reached with a radius of $\sqrt{0.5}$ AU. (d) The polar orbit phase about Alpha Centauri B. The polar orbit is reached in 4.5 years and the total transfer time for the exploration mission of the $\alpha$Cen system is about 32 years. Finally, a preliminary analysis of the variation of the Zero Velocity Curves has been performed, showing the efficiency of both the capture and the transfer phases from $\alpha$CenA to $\alpha$CenB.

After that, a more actual space mission has been considered to analysing the astrodynamical behaviour of a sailcraft for space weather, specifically for early warning of Coronal Mass Ejection-induced solar storms. Such mission would allow achieving a long warning time of 140 minutes in the fast-streams environment. To such a purpose, in the first part of the section, we have introduced the concept of sailcraft synchronous with the Earth-Moon barycentre via several assumptions, and carried out the proper lightness number, a necessary condition for synchrony. This value depends non-linearly on the desired early warning time. Increasing the warning time, as given by the ACE/NASA spacecraft, entails to achieve an orbit remarkably lower than the Sun-Earth L1 point, well lower than any halo orbit related to L1. The technology related to all sailcraft systems is needed to be much more advanced than those ones used for IKAROS JAXA and NanoSail-D2/NASA. The spontaneous motion of the sailcraft under the gravitational perturbations of the near planets would cause a strong loss of synchrony if not counterbalanced. This could be done with no propellant consumption by tilting the sail slightly with respect to the local direction of sunlight. We introduced the concept of baseline synchrony profile whereupon the nominal synchronous orbit turns to a piecewise-constant attitude control in the sailcraft heliocentric orbital frame. Controlling the sail not only radially, but also transversally (pitch angle control), results in the annual mean synchrony; in other words, we need to restrict the motion spread of the sailcraft, as seen from the Earth during a year. Each operational year has its own sequence of four attitude re-orientation manoeuvres; in this thesis, we have analysed the year from July 2022 to July 2023.

Then, a parametric transfer orbit to Mercury and to Mars is taken in account to evaluate the variation of time of flight to reach the target varying the sailcraft performance. The two selected reflection model are the specular and the Fresnel one. The entire comparison between these reflection model empathize the importance of a accurate model for the mission design. A different reflection model could introduce an important deviation from the optimal trajectory obtained with another one. This analysis empathizes that exists a divergence in the time of flight between the two reflection models reducing the performance of the sailcraft, in the specific a no-linear behaviour is present in both mission time of flight. For a certain range of characteristic acceleration the difference between both reflection model increase significantly to decrease again.

Finally an experimental analysis has been set up. We design an instrument that uses a laser beam sensor to measure the distance between itself and the membrane and it moves by a set of stepper motors over two axes. Three samples of solar sail material - 2 $\mu$m CP1 - with the same aluminium coating - 100nm - have been prepared with a Kapton support on the vertexes and three eyelets for each samples used to apply tension to the samples. Three representative tensional cases have been selected to an probability distribution analysis and a probability density function has been carried out. These result on distribution of wrinkles and creases have been applied to three optimal trajectory before calculated to Mercury to evaluate the impact of these effect on the trajectory. An optimization considering the deformation parameters has been evaluated to compare the effect on the time of flight. An increasing on the time of flight has been produced and this confirm that the local surface deformations affect the trajectory in a not negligible way. Future work shall take deformations into account for accurate analyses of solar sail missions.

# A

# Appendix A

All the passages to obtain the equation for the ER3BP are following listed:

$$\rho' = \frac{ep\sin\nu}{g^2} \tag{1.0.1}$$

$$\rho'' = \frac{ep\cos\nu}{g^2} + \frac{2e^2 p\sin^2\nu}{g^3} \tag{1.0.2}$$

$$\dot{\omega} = -2e\frac{h^2}{\rho^4}\sin\nu g^3 \tag{1.0.3}$$

$$x = \rho\xi \quad y = \rho\eta \quad z = \rho\zeta \tag{1.0.4}$$

$$\dot{x} = \omega\left(\rho'\xi + \rho\xi'\right) \tag{1.0.5}$$

$$\dot{y} = \omega\left(\rho'\eta + \rho\eta'\right) \tag{1.0.6}$$

$$\dot{z} = \omega\left(\rho'\zeta + \rho\zeta'\right) \tag{1.0.7}$$

$$\ddot{x} = \omega^2\left(\rho''\xi + 2\rho'\xi' + \rho\xi''\right) + \dot{\omega}\left(\rho'\xi + \rho\xi'\right) \tag{1.0.8}$$

$$\ddot{y} = \omega^2\left(\rho''\eta + 2\rho'\eta' + \rho\eta''\right) + \dot{\omega}\left(\rho'\eta + \rho\eta'\right) \tag{1.0.9}$$

$$\ddot{z} = \omega^2\left(\rho''\zeta + 2\rho'\zeta' + \rho\zeta''\right) + \dot{\omega}\left(\rho'\zeta + \rho\zeta'\right) \tag{1.0.10}$$

Making a substitution of Eqs. (1.0.1)–(1.0.3) into Eq. (1.0.4):

$$x = \frac{p}{g}\xi \tag{1.0.11}$$

$$\dot{x} = \frac{h}{p}\left(e\sin\nu\xi + g\xi'\right) \tag{1.0.12}$$

$$\ddot{x} = \xi''\left(\frac{h^2}{p^3}g^3\right) + \xi\left(\frac{h^2}{p^3}eg^3\cos\nu\right) \tag{1.0.13}$$

$$y = \frac{p}{g}\eta \tag{1.0.14}$$

$$\dot{y} = \frac{h}{p}\left(e\sin\nu\eta + g\eta'\right) \tag{1.0.15}$$

$$\ddot{x} = \eta''\left(\frac{h^2}{p^3}g^3\right) + \eta\left(\frac{h^2}{p^3}eg^3\cos\nu\right) \tag{1.0.16}$$

$$z = \frac{p}{g}\zeta \tag{1.0.17}$$

$$\ddot{z} = \zeta''\left(\frac{h^2}{p^3}g^3\right) + \zeta\left(\frac{h^2}{p^3}eg^3\cos\nu\right) \tag{1.0.18}$$

# Bibliography

[1] T. Pino and C. Circi. A star-photon sailcraft mission in the alpha centauri system. *Advances in Space Research*, 59(9):2389 – 2397, 2017. ISSN 0273-1177. doi:10.1016/j.asr.2017.02.014.

[2] G. Vulpetti, C. Circi, and T. Pino. Coronal mass ejection early-warning mission by solar-photon sailcraft. *Acta Astronautica*, 140:113 – 125, 2017. ISSN 0094-5765. doi:10.1016/j.actaastro.2017.07.042.

[3] Robert Gershman and Calina Seybold. Propulsion trades for space science missions. 45:541–548, 08 1999. doi:10.1016/S0094-5765(99)00174-5.

[4] Manfred Leipold, Dieter Kassing, M Eiden, and L Herbeck. Solar sails for space exploration - the development and demonstration of critical technologies in partnership. pages 102–107, 06 1999. URL `http://www.esa.int/esapub/bulletin/bullet98/LEIPOLD.pdf`.

[5] Esther Morrow, D Scheeres, and Dan Lubin. Solar sail orbit operations at asteroids. 38(2):279–286, 04 2001. doi:10.2514/2.3682.

[6] Giuseppe Racca. New challenges to trajectory design by the use of electric propulsion and other new means of wandering in the solar system. 85:1–24, 01 2003. doi:10.1023/A:1021787311087.

[7] Manfred Leipold, H Fichtner, B Heber, P Groepper, S Lascar, F Burger, M Eiden, T Niederstadt, C Sickinger, L Herbeck, Wolfgang Seboldt, Bernd Dachwald, G Hughes, and C McInnes. Heliopause explorer - a sailcraft mission to the outer boundaries of the solar system. pages 785–796, 01 2003. doi:10.1016/j.actaastro.2005.07.024.

[8] C.G. Sauer Jr. Solar sail trajectories for solar polar and interstellar probe missions. 103:99–336, 01 2000. URL `https://trs.jpl.nasa.gov/bitstream/handle/2014/17917/99-1367.pdf?sequence=1`.

[9] J. L. Anderson. Roadmap to a star. *Acta Astronautica*, 44(2):91 – 97, 1999. doi:10.1016/S0094-5765(99)00033-8.

[10] C.R McInnes. Delivering fast and capable missions to the outer solar system. 34:184–191, 12 2004. doi:10.1016/j.asr.2003.02.063.

[11] J. L. Wright. *Space sailing.* Philadelphia : Gordon and Breach Science Publishers, 1992. ISBN 2881248039 (hardcover). URL `https://trove.nla.gov.au/work/11497003`. pp. 227—233.

[12] G. Vulpetti. *Fast Solar Sailing: Astrodynamics of Special Sailcraft Trajectories, Space Thecnology Library.* Springer, 2012. doi:10.1007/978-94-007-4777-7.

[13] G. Vulpetti, L. Johnson, and G. L. Matloff. *Solar Sails: A Novel Approach to Interplanetary Travel.* Springer-Verlag New York, 2015. doi:10.1007/978-1-4939-0941-4.

[14] C. Gueymard. The sun's total and spectral irradiance for solar energy applications and solar radiation models. 76:423–453, 04 2004. doi:10.1016/j.solener.2003.08.039.

[15] C. H. M. Jenkins. Recent advances in gossamer spacecraft. 01 2006. doi:10.2514/4.866814.

[16] N.H. Mcclamroch. Space vehicle dynamics and control. 37:2077–2078, 12 2001. doi:10.1016/S0005-1098(01)00163-7.

[17] G.L. Matloff, G. Vulpetti, C. Bangs, and R. Haggerty. *Interstellar Probe (ISP): Pre- perihelion Trajectories and Application of Holography.* NASA/CR 2002–211730, 2002. URL `http://wayback.archive-it.org/1792/20100214112751/http://ntrs.nasa.gov/archive/nasa/casi.ntrs.nasa.gov/20020073860_2002123101.pdf`.

[18] G. Vulpetti. Effect of the total solar irradiance variations on solar-sail low-eccentricity orbits. *Acta Astronautica*, 67(1):279 – 283, 2010. ISSN 0094-5765. doi:10.1016/j.actaastro.2010.02.004.

[19] P. Gurfil and D. Meltzer. Stationkeeping on unstable orbits: Generalization to the elliptic restricted three-body problem. *The Journal of the Astronautical Sciences*, 54(1):29–51, 2006. doi:10.1007/BF03256475.

[20] V. Szebehely and C. F. Peters. A new periodic solution of the problem of three bodies. *Astronimical Journal*, 72:1187, November 1967. doi:10.1086/110398.

[21] `https://www.iers.org/IERS/EN/Home/home_node.html`.

[22] A. E. Roy. *Orbital motion 4th edition*. Institute of Physics Publishing, 2005.

[23] G. Mengali and A. A. Quarta. Solar sail trajectories with piecewise-constant steering laws. *Aerospace Science and Technology*, 13(8):431 – 441, 2009. doi:10.1016/j.ast.2009.06.007.

[24] A. A. Quarta and G. Mengali. Optimal switching strategy for radially accelerated trajectories. *Celestial Mechanics and Dynamical Astronomy*, 105(4):361–377, 2009. doi:10.1007/s10569-009-9233-2.

[25] L. Niccolai, A. A. Quarta, and G. Mengali. Analytical solution of the optimal steering law for non-ideal solar sail. *Aerospace Science and Technology*, 62:11 – 18, 2017. doi:10.1016/j.ast.2016.11.031.

[26] G. L. Pilbratt. Herschel space observatory mission overview. *SPIE*, 4850(586–597), 2003. doi:10.1038/srep06484.

[27] S. Triqueneaux, L. Sentis, Ph. Camus, A. Benoit, and G. Guyot. Design and performance of the dilution cooler system for the planck mission. *Cryogenics*, 46(4):288 – 297, 2006. ISSN 0011-2275. doi:10.1016/j.cryogenics.2005.12.004.

[28] A. D. Rougier, C. Danine, and S. B. Faure. Cylindrical manifolds and tube dynamics in the restricted three-body problem. *Ph.D. thesis, California Institute of Technology*, 2004. URL `http://resolver.caltech.edu/CaltechETD:etd-05182004-154045`.

[29] Martin Lo, Bobby Williams, Williard Bollman, Dongsuk Han, Yungsun Hahn, Julia Bell, Edward Hirst, Robert Corwin, Philip Hong, Kathleen Howell, and al e. Genesis mission design. 49:169–184, 2001.

[30] Marc D. Rayman, Thomas C. Fraschetti, Carol A. Raymond, and Christopher T. Russell. Coupling of system resource margins through the use of electric propulsion: Implications in preparing for the dawn mission to ceres and vesta. *Acta Astronautica*, 60(10):930 – 938, 2007. ISSN 0094-5765. doi:10.1016/j.actaastro.2006.11.012.

[31] Guibout, V. and Scheeres, D. . Periodic orbits from generating functions. *Advances in the Astronautical Sciences*, 116(2):1029–1048, 2004.

[32] Russell Eberhart and James Kennedy. *A new optimizer using particle swarm theory.* 1995.

[33] Je rey Horn, Nicholas Nafpliotis, and David E Goldberg. *A niched Pareto genetic algorithm for multiobjective optimization*, volume 1. 1994.

[34] T Zhu and SN Atluri. A modified collocation method and a penalty formulation for enforcing the essential boundary conditions in the element free galerkin method. *Computational Mechanics*, 21(3):211–222, 1998.

[35] P. E. Gill, W. Murray, and M. A. Saunders. Snopt: An sqp algorithm for large-scale constrained optimization. *SIAM Review*, 47(1):99–131, 2005. doi:10.1137/S0036144504446096.

[36] M. Yıldız. Solar and $\alpha$ centauri a and b models improved by opacity enhancement – a possible explanation for oversize cool stars. *Monthly Notices of the Royal Astronomical Society*, 412(4):2571–2578, 2011. doi:10.1111/j.1365-2966.2010.18075.x.

[37] P. Thébault, F. Marzari, and H. Scholl. Planet formation in $\alpha$ centauri a revisited: not so accretion friendly after all. *Monthly Notices of the Royal Astronomical Society*, 388(4):1528–1536, 2008. doi:10.1111/j.1365-2966.2008.13536.x.

[38] E. Andrade-Ines and T. A. Michtchenko. Dynamical stability of terrestrial planets in the binary centauri system. *Monthly Notices of the Royal Astronomical Society*, 444(3):2167–2177, 2014. doi:10.1093/mnras/stu1591.

[39] X. Dumusque, F. Pepe, C. Lovis, D. Ségransan, J. Sahlmann, W. Benz, F. Bouchy, M. Mayor, D. Queloz, N. Santos, and S. Udry. An earth-mass planet orbiting $\alpha$ centauri b. *Nature*, 491:207–211, 2012. doi:10.1038/nature11572.

[40] B.O. Demory, D. Ehrenreich, D. Queloz, S. Seager, R. Gilliland, W. J. Chaplin, C. Proffitt, M. Gillon, M. N. Günther, B. Benneke, X. Dumusque, C. Lovis, F. Pepe, D. Ségransan, A. Triaud, and S. Udry. Hubble space telescope search for the transit of the earth-mass exoplanet $\alpha$ centauri b b. *Monthly Notices of the Royal Astronomical Society*, 450(2):2043–2051, 2015. doi:10.1093/mnras/stv673.

[41] D. Forgan. Oscillations in the habitable zone around $\alpha$ centauri b. *Monthly Notices of the Royal Astronomical Society*, 422(2):1241–1249, 2012. doi:10.1111/j.1365-2966.2012.20698.x.

[42] A. Bond and A. R. Martin. Project daedalus: The mission profile. *The British Interplanetary Society*, 1(SUPPL.):S37–S42, 1978. URL `http://adsabs.harvard.edu/abs/1978JBIS...31S..37B`.

[43] Thèvenin, F., Provost, J., Morel, P., Berthomieu, G., Bouchy, F., and Carrier, F. Asteroseismology and calibration of $\alpha$cen binary system. *Astronomy and Astrophysics*, 392(1):L9–L12, 2002. doi:10.1051/0004-6361:20021074.

[44] J. Anosova, V.V. Orlov, and N.A. Pavlova. Dynamics of nearby multiple stars. the alpha centauri system. *Astronomy and Astrophysics*, 292: 115–118, dec 1994. URL `http://adsabs.harvard.edu/abs/1994A%26A...292..115A`.

[45] Nordström, B., Mayor, M., Andersen, J., Holmberg, J., Pont, F., Jorgensen, B. R., Olsen, E. H., Udry, S., and Mowlavi, N. The geneva-copenhagen survey of the solar neighbourhood. *Astronomy and Astrophysics*, 418(3):989–1019, 2004. doi:10.1051/0004-6361:20035959.

[46] Pourbaix, D., Nidever, D., McCarthy, C., Butler, R. P., Tinney, C. G., Marcy, G. W., Jones, H. R. A., Penny, A. J., Carter, B. D., Bouchy, F., Pepe, F., Hearnshaw, J. B., Skuljan, J., Ramm, D., and Kent, D. Constraining the difference in convective blueshift between the components of $\alpha$ centauri with precise radial velocities. *Astronomy and Astrophysics*, 386(1):280–285, 2002. doi:10.1051/0004-6361:20020287.

[47] G. Mengali and A. A. Quarta. Solar sail near-optimal circular transfers with plane change. *Journal of Guidance, Control, and Dynamics*, 32 (2):456 – 463, 2009. doi:10.2514/1.38079.

[48] A. A. Quarta and G. Mengali. Approximate solutions to circle-to-circle solar sail orbit transfer. *Journal of Guidance, Control, and Dynamics*, 36(6):1886 – 1890, 2013. doi:10.2514/1.60307.

[49] C. Circi and P. Teofilatto. Effect of planetary eccentricity on ballistic capture in the solar system. *Celestial Mechanics and Dynamical Astronomy*, 93(1):69–86, 2005. doi:10.1007/s10569-005-3640-9.

[50] D. Romagnoli and C. Circi. Earth–moon weak stability boundaries in the restricted three and four body problem. *Celestial Mechanics and*

*Dynamical Astronomy*, 103(1):79–103, 2009. doi:10.1007/s10569-008-9169-y.

[51] C.R. McInnes. *Solar Sailing: Technology, Dynamics and Mission Applications*. Springer-Verlag Berlin Heidelberg, 2004.

[52] G. Vulpetti. *Applying Vector Scattering Theory to Solar-Photon Sail Thrust Modeling*, pages 489–508. Springer Berlin Heidelberg, 2014. doi:10.1007/978-3-642-34907-2_31.

[53] J. Heiligers, M. Macdonald, and J. S. Parker. Extension of earth-moon libration point orbits with solar sail propulsion. *Astrophysics and Space Science*, 361(7):241. doi:10.1007/s10509-016-2783-3.

[54] E. R. Priest and T. Forbes. *Magnetic reconnection. MHD theory and applications*. Cambridge University Press, 2000. ISBN 0-521-48179-1.

[55] K. Schindler and G. Hornig. Magnetic reconnection. *Encyclopedia of astronomy and astrophysics*, pages 1517–1524. doi:10.1888/0333750888/2224.

[56] N. Meyer-Vernet. *Basics of the Solar Wind*. Cambridge University Press, January 2007.

[57] J. Bookless and C. McInnes. Control of lagrange point orbits using solar sail propulsion. *Acta Astronautica*, 62(2):159 – 176, 2008. ISSN 0094-5765. doi:10.1016/j.actaastro.2006.12.051.

[58] J. Heiligers, G. Mingotti, and C. R. McInnes. Optimal solar sail transfers between halo orbits of different sun-planet systems. *Advances in Space Research*, 55(5):1405 – 1421, 2015. ISSN 0273-1177. doi:10.1016/j.asr.2014.11.033.

[59] G. Vulpetti, S. Santoli, and G. Mocci. Preliminary Investigation on Carbon Nanotube Membranes for Photon Solar Sails. *Journal of the British Interplanetary Society*, 61:284–289, 2008.

[60] G. Vulpetti and C. Circi. Mass breakdown model of solar-photon sail shuttle: The case for mars. *Acta Astronautica*, 119:87 – 100, 2016. ISSN 0094-5765. doi:10.1016/j.actaastro.2015.11.010.

[61] E.L. Church and P.Z. Takacs. *Surface Scattering, Chap. 7 of Handbook of Optics, third ed., vol. I*. McGraw-Hill, 2010.

[62] A.A. Quarta and G. Mengali. Solar sail missions to mercury with venus gravity assist. *Acta Astronautica*, 65(3):495 – 506, 2009. ISSN 0094-5765. doi:10.1016/j.actaastro.2009.02.007.

[63] G. Vulpetti. Total solar irradiance fluctuation effects on sailcraft-mars rendezvous. *Acta Astronautica*, 68(5):644 – 650, 2011. ISSN 0094-5765. doi:10.1016/j.actaastro.2010.01.010. Special Issue: Aosta 2009 Symposium.

[64] D. Zola, C. Circi, G. Vulpetti, and S. Scaglione. Photon momentum change of quasi-smooth solar sails. *J. Opt. Soc. Am. A*, 35(8):1261–1271, Aug 2018. doi:10.1364/JOSAA.35.001261.

[65] G. Greschik and M. M. Mikulas. Design study of a square solar sail architecture. *Journal of Spacecraft and Rockets*, 39, 09 2002. doi:10.2514/2.3886.

[66] J. Wang, T. Chen, D. Sleight, and A. Tessler. 45th AIAA/ASME/ASCE/AHS/ASC structures, structural dynamics & materials conference - simulating nonlinear deformations of solar sail membranes using explicit time integration. 2004. ISBN 978-1-62410-079-6. doi:10.2514/6.2004-1580.

[67] L. Rios-Reyes and D. J. Scheeres. Generalized model for solar sails. *Journal of Spacecraft and Rockets*, 42, 01 2005. doi:10.2514/1.9054.

[68] Hiraku Sakamoto, Yasuyuki Miyazaki, and K. C. Park. Finite element modeling of sail deformation under solar radiation pressure. *Journal of Spacecraft and Rockets*, 44, 05 2007. doi:10.2514/1.23474.

[69] W. Wong and S. Pellegrino. Wrinkled membranes part i: Experiments. 1:3–25, 05 2006. doi:10.2140/jomms.2006.1.3.